Hypervelocity Impact Simulation using Smoothed-Particle Hydrodynamics

Mateusz Harazim

Delft University of Technology

TU Delft

Hypervelocity Impact Simulation using Smoothed-Particle Hydrodynamics

by

Mateusz Harazim

Student Name	Student Number
Mateusz Harazim	4656377

Supervisor:	Prof. Chiara Bisagni
Co-Supervisor:	Ing. Tiziana Cardone
Project Duration:	May, 2022 - February, 2023
Faculty:	Faculty of Aerospace Engineering, Delft

Cover: 'Gravity' directed and produced by Alfonso Cuarón. Distributed by Warner Bros Pictures. Related on August 28, 2013, in Venice.

TU Delft

Summary

The issue of space debris in Low Earth Orbit is a growing concern that requires comprehensive solutions. This includes preventing further pollution, removing existing debris, and designing resilient spacecraft that can withstand impacts. One important aspect of this is the improvement of spacecraft shielding structures to provide effective protection and allow the spacecraft to continue its mission even after being hit by debris. This not only saves the mission but also prevents the spacecraft from becoming additional debris. Objects in orbit greater than 1cm are tracked and could be avoided. Smaller objects are currently not possible to effectively follow. Nevertheless, even small objects colliding at orbital velocities can have serious consequences. They are called hypervelocity impacts, as they occur at relative velocities between 2 and 10 km/s .

A Whipple shield is an effective method of dispersing the energy of the collision. They are made from multiple plates, where the first one gets penetrated and disperses the projectile into smaller fragments. The plates following can then resist this cloud of particles much more easily.

Testing and development of such a shield are difficult and expensive. The numerical approach is needed to perform a more comprehensive optimization of the design. This thesis examines the Smoothed-Particle Hydrodynamics method of simulation of hypervelocity impacts using LS-DYNA. The method is currently preferred in literature for the simulation of impacts at high velocity, thanks to the ability to represent clouds of fragments much better than the Finite Element Method.

Two studies from the past were reproduced in order to confirm the validity of the SPH model. Both studies from Plassard et al. and Legaud et al. were successfully replicated in the same order of accuracy as the originals. The focus of the studies was on the effects of impact on a single metal plate.

Next, the simulation was performed on a double plate system. The primary plate was modelled using 691200 SPH particles formed in a square of dimensions 30 x 30 mm. The second plate was modelled using 1225000 SPH particles in a square of 100 x 100 mm. The square was surrounded by a frame of 95424 FEM elements, increasing the total plate size to 300 x 300 mm. The impacting sphere with a 5 mm diameter consists of 33552 SPH. The results were compared with the data from experiments provided by Airbus Defence and Space GmbH. Overall, four experiments were simulated at impact velocities from 2.9 to 7.1 km/s. The projectile was Al 2007 sphere with a 5mm diameter and the target was a two-plate Whipple shield made out of Al 2024-T3 with a thickness of 0.8mm. In this setup, all shields were fully perforated. The comparison was made between the crater diameters in the experiments and the simulation.

The simulation accurately predicted the hole diameter in the 1st plate, with less than 2% error. The damage zone in the second plate has been much more varied, just like in the experimental data provided. The discrepancy between simulation and experiments for the 2nd plate ranged from 10% to over 100%. One of the experiments was an outlier with an exceptionally small second crater. There is considerable variance in the damage zone size of the secondary crater. The simulations consistently overpredict the damage zone, leading to conservative results. During the development of the simulation, an error was found in the LS-DYNA solver causing energy loss. After testing and consultation with developers, it was concluded that it likely has minimal effect on the measured parameters. This error will be repaired in future LS-DYNA releases.

Contents

Nomenclature

Abbreviations

Abbreviation	Definition
AIAA	American Institute of Aeronautics and Astronautics
BC	Boundary condition
CFRP	Carbon Fibre Reinforced Polymer
CST	Collision Simulation Tool
EOS	Equation Of State
ESA	European Space Agency
FE	Finite Element
FEM	Finite Element Method
LEO	Low Earth Orbit
MMALE	Multi Material Arbitrary Lagrangian Eulerian Method
NASA	National Aeronautics and Space Administration
PIRAT	Particle Impact Risk and Vulnerability Analysis Tool
SBM	Standard Breakup Model
SPH	Smoothed-Particle Hydrodynamics

Symbols

Symbol	Definition
γ	Gruensen Parameter $(-)$
ϵ_p	Plastic strain $(-)$
$\dot{\epsilon}/\dot{\epsilon_0}$	Normalised equivalent plastic strain rate $(-)$
ρ	Density $(Mass/Length^3)$
ξ	Ratio of distance from the centre of particle to the smoothing length $(Length/Length)$
Ω	d-dimensional smoothing domain $(Length^d)$
Ep	Ratio of projectile energy to the mass of spacecraft $(Length^2/(Time^2))$
h	smoothing length $(Length)$
$m_{projectile}$	Mass of projectile $(Mass)$
m_{target}	Mass of the affected components of spacecraft during impact $(Mass)$
v_{impact}	Relative velocity of objects at impact $(Mass/Length)$
a	Tillotson parameter $(-)$
A	Johnson-Cook parameter $(Mass/(Length * Time^2))$
B	Johnson-Cook parameter $(Mass/(Length * Time^2))$
c	Johnson-Cook parameter $(-)$
c	Sound speed $(Length/Time)$
C	Specific heat $(Length^2 * Temperature/(Time^2))$
C	B-Spline function constant $(-)$
C	Gruneisen EOS parameter $(-)$t
D1	Johnson-Cook fracture parameter $(-)$
D2	Johnson-Cook fracture parameter $(-)$
D3	Johnson-Cook fracture parameter $(-)$
D4	Johnson-Cook fracture parameter $(-)$
D5	Johnson-Cook fracture parameter $(-)$
D_{1st}	Diameter of the crater in the first plate $(-)$t
D_{2nd}	Diameter of the crater in the second plate $(-)$t
E	Internal energy $(Mass * Length^2/(Time^2 * Mass))$
k	Specific heat ratio $(-)$
L	Debris cloud length $(Length)$
n	Johnson-Cook parameter $(-)$
m	Johnson-Cook parameter $(-)$
P	Pressure $(Mass/(Length * Time^2))$
R	Ideal gas constant $(Length^2 * Temperature/(Time^2))$
S1	Gruneisen EOS parameter $(-)$
S2	Gruneisen EOS parameter $(-)$

Symbol	Definition
S3	Gruneisen EOS parameter $(-)$
T	Temperature $(Temperature)$
V	Velocity $(Length/Time)$
V_{max}	Maximum velocity of the debris cloud

1

Acknowledgments

I would like to thank Airbus Defence and Space GmbH for providing the data used for the validation of the simulation in my thesis. Without their contribution, the scientific value of the thesis would be diminished. I would like to express my gratitude to prof. Chiara Bisagni, for enabling me to work on a such an exciting topic. I am also thankful to Tiziana Cardone. This area of research at the university would not be possible without her determination in pursuing this subject despite the multitude of responsibilities at the European Space Agency. Furthermore, thanks to Javier Paz Méndez, who helped me to break through barriers on a way to the completion of the thesis.

My journey would not be possible without unending support from my family. Starting with my parents, Mariola and Marek Harazim, who have backed years of my education and helped me in all ways possible. Furthermore, thanks to Justyna, Jan and Antonina Czerwińscy for the support throughout my whole life. Finally, I want to express my gratitude to my grandmother Teresa Mocha, who has been a constant support and was especially helpful to me during the first year of my master's degree, which I completed from my hometown in Poland. In addition, I would like to thank my Aikido trainer Krzysztof Puchalski, who has shaped me into who I am today. The instilled discipline has contributed tremendously to my success during my years in the Netherlands.

I would like to thank my friends from all paths of life, who have all contributed to my development and well-being. Special thank you to everyone who has worked with me side by side at the University, reminding me that I am not alone in this journey.

2

Problem description

Space exploration has been experiencing big growth over the last decades. After a multitude of innovations in the cold war era and relative stagnation in the 90s, currently, the New Space is growing. Decentralization and the use of new technologies are making spaceflight more accessible, with potential benefits for scientific research, commercial services, and military operations. Satellites can provide valuable data on climate, physics, and astronomy, while also offering services such as fast internet, telecommunications, and navigation.
The increasing use of spacecraft for various purposes has led to the need for more satellites to be placed in orbit. As society becomes more dependent on these services, the need to launch more satellites is expected to continue. However, this trend also highlights the importance of sustainability in the space industry.
Humans have been launching objects into space for over 65 years, and the frequency of these launches has been increasing. As a result, the space around Earth is becoming increasingly crowded. While this was not initially a problem, it has become a more pressing issue over time. Objects at lower orbits progressively decay and eventually fall to burn in the atmosphere. On the other hand, spacecraft in higher orbits could remain there for a very long time, possibly hundreds or even thousands of years. The progression of the space sector is occurring at a speed that is an order of magnitude faster.
One of the main challenges in maintaining a sustainable space environment is the increasing amount of debris in orbit. Debris is defined as any human-made object in orbit that is no longer serving any useful purpose. This includes old satellites, rocket stages, and fragments that have been created by collisions or explosions in space.
The generation of debris is heavily dependent on the capability to discard the used satellites into an area that will not obstruct the newer spacecraft. This has been noticed in the past and policies were implemented to ensure that the spacecraft would be discarded in two main ways. For objects in Low Earth Orbit (LEO), it was required for the spacecraft to be de-orbited within 25 years of the end of the mission. For objects in higher orbits, special Graveyard orbits were distinguished to direct the spacecraft at the end of its life there. Those rules were aimed to reduce the impact of the debris on future missions, but they are not sufficient anymore. This is why in 2022 the new law was approved to reduce this decommission time at LEO to only 5 years [1], and considerable research is conducted to mitigate the effects of orbit overcrowding.
The space debris is not limited to the complete spacecraft in the orbit. In addition to whole satellites, smaller objects such as paint flakes, discarded components, and fragments of old craft also pose a danger to other spacecraft. The disintegration of just one satellite can result in the creation of thousands or even millions of these small, hazardous elements. While there is a small and stable number of natural objects, such as micro meteors, the rapidly growing amount of human-made debris is a more pressing concern.

Space debris can be classified into different size categories based on its rough dimensions. Radars on Earth's surface track and count the number of objects in orbit, the majority of which are debris. The size of the object is a determining factor as radars have limited resolution through the atmosphere, which

limits their ability to detect smaller pieces of debris. The current estimates indicate that the number of objects above 1 cm is ranging between 100 000 to 200 000 [2]. From that, around 5000 are functioning satellites - a number that has doubled since 2019. Figure 2.1 pictures the distribution of debris in orbit.

Figure 2.1: Representation of tracked space debris larger than 1mm. Satellites (red), rocket bodies (yellow), fragments (blue) and auxiliary mission-related objects (green) and shown. Courtesy of European Space Agency.

The rapid raise in the number of spacecraft is partly related to a new type of space mission. High-density constellations counting thousands of satellites are now possible thanks to miniaturisation and affordable launches. Most spacecraft, including those used in mega constellations, are launched into Low Earth Orbit. It is the easiest orbit to reach and has lots of advantages that include small communication delay and high resolution for imaging instruments.
New space missions have to consider the risks of debris hitting the spacecraft. The larger pieces that are tracked are often avoided using evasive manoeuvres if the spacecraft has such capability. However, the even smaller fragment can pose a danger to the craft if not accounted for.
In the worst-case scenario, this threat will become more and more serious. With each collision, more debris is added to the pool that could become a problem for the next missions. That could lead to an exponential growth of the debris in the Low Earth Orbit. That sets humanity on the path to the so-called Kessler syndrome - a phenomenon where the amount of space debris is so high, that space travel becomes near impossible due to collision risk. In the end stages of such an event, the majority of spacecraft is to be ground into a powder that remains in orbit for an extended time, colliding and destroying any object that escapes the atmosphere.
The relative velocity between two objects in different orbits can be very large. Objects that sustain circular orbit at LEO travel at 7.8km/s. Therefore, impacts between them involve speeds that are not seen on Earth. Even small pieces of debris can have devastating effects, with larger objects bringing almost a certain end to the spacecraft. Such events are classified as hypervelocity impacts. As they are becoming more common, it is now a standard practice in mission design to develop risk mitigation measures for that case. It includes path planning to avoid zones of high debris concentration, possible evasive manoeuvres and design of appropriate shielding for smaller impacts. As mentioned before, objects small enough cannot be tracked and therefore cannot be avoided. However, the energy of the impact is comparable with the hand grenade explosion even for debris smaller than 1cm. The kinetic energy scales with the square of the velocity and it is very high for such impacts. Efficient shielding increases the margin of error and allows mission planners more freedom in pathing. If certain hits can be absorbed without compromising the mission, it greatly increases the odds of survival. Additionally,

it potentially could lead to lighter spacecraft as less propellant is used for evasive manoeuvres.
The material behaves differently when struck at such speed, with behaviour more like a fluid. The pressure involved at the impact zone is well beyond the yield strength of the material. Therefore, the creation of resilient shielding is a challenging task. Whipple shields are the standard method of protection. They consist of multiple layers of structural material separated by a distance. This enables the first layer to disperse the object into smaller pieces, with secondary layers being able to absorb the impact over a larger area. The use of multiple thin shields saves mass and relates to another common spacecraft element - sandwich structure. Having exceptional bending stiffness and strength, built from sheets of stiff material separated by a low-density filler such as honeycomb. Spacecraft designers combine properties of both creating a Whipple shield that works as a structural element within the spacecraft. Therefore, in the design process, the requirement of hypervelocity impact protection plays an important role. The structure shall contain the impact and not let the jet of velocity debris damage internal components.
The design of such a shield is difficult due to the limited availability of testing facilities. Experimentation in space is not possible and would be counterproductive. Therefore, the experiments have to be conducted in hypervelocity research facilities, which make use of light-gas guns to accelerate the projectiles to such high speeds. Such guns accelerate projectiles to up to 10km/s using multiple-stage compression and combustion. There is a limited number of such facilities in the world, and their operation is very expensive. That encourages the development of simulation techniques that expand the possibilities of iteration and development of new shields. Simulations can be used to evaluate a much wider array of impact scenarios, ideally creating an operational envelope of hypervelocity impacts resilience for a given spacecraft. This can be used during operations to better inform the operators of decisions on evasive manoeuvres.

2.1. Research question

The thesis aims to create a simulation technique that can be used for the development of Whipple Shields for spacecraft. The simulation is validated using the latest experiments provided by the European Space Agency, courtesy of Airbus Defence and Space GmbH. The goal is the creation of a simulation procedure that enables an accurate representation of the projectile impact over a wide range of velocities present in orbit. As a part of a larger spacecraft debris mitigation programme, it enhances the ability of designers and operators to deal with this emerging threat.
The goal of the research is to create a simulation that is capable of accurately predicting the diameter of the damage zone after a hypervelocity impact into a two-layer aluminium Whipple shield. With the use of the Smoothed-Particle Hydrodynamics method, the simulation shall be able to model the interaction between all different parts consistently, allowing for an accurate prediction of the diameter of the damage zone.
This information can be used for the design and optimization of hypervelocity impact protection systems for spacecraft. Experimental data will be utilized to compare the simulation's findings to the actual results of the hypervelocity impact. This will provide an evaluation of the accuracy and reliability of the simulation in predicting the diameter of the damage zone. Overall, this research aims to contribute to the understanding of hypervelocity impact phenomena and to provide a tool for the design and optimization of protection systems for objects exposed to high-speed debris in the space environment.
The specific contribution of this work to the field is the creation of a detailed simulation of a two-plate system that accurately captures the damage zone at a wide range of speeds from 2.9 to 7.2 km/s. The validation of the simulaton uses the experimental values from imapcts on aluminium Whipple shields. The simulation of those specific experiments enables a direct comparison between the damaged site in the simulation and actual events conducted at a state-of-the-art facility.
The simulation is conducted using LS-DYNA, a powerful software that simulates the response of structures and materials under dynamic conditions. It is widely used in the aerospace and automotive industries to analyze the behaviour of structures during impacts, explosions, and other types of transient loading. LS-DYNA uses both FEM and SPH to solve highly non-linear problems, and it has the ability to model metals, composites, complex geometries, contact between multiple components, and large deformations. As it can model dynamic events such as shock waves and high-speed deformation, it is a suitable choice for simulating hypervelocity impact. LS-DYNA has been found to be the most

successful software for performing hypervelocity simulations in the literature [3].
The simulation serves as one of the components in the future space sustainability programme, encompassing the use of experimental, semi-empirical and numerical techniques for debris danger mitigation. Components involved in the programme are the following: detection, prevention, avoidance, impact mitigation and possibly removal. This research is a part of the numerical impact mitigation measures, used to simulate the effects of the impact on the spacecraft. It serves as the cornerstone for further work on the numerical simulation of larger spacecraft components for penetration resistance and durability.

3

Literature

This chapter provides an overview of the existing research on hypervelocity impact simulation. A comprehensive summary of the current state-of-the-art is presented and the key findings and advances are highlighted It covers three branches of research, including experimental studies, semi-empirical models, and numerical simulations.
It then goes on to discuss the different numerical methods used in previous studies and the advantages and limitations of each respectively. The literature review chapter provides a basis for further work by introducing the background of important findings that this work is based upon.

3.1. Experimental

Experiments of hypervelocity impacts in space are challenging for practical reasons. The ability to extract data from experiments performed in orbit would severely inhibit the useful results. Moreover, such experimentation would cause additional accumulation of debris, worsening the problem. Therefore, on-ground testing is the main way of experimentation available. It is used to study the performance of components under such impacts as well as to study the underlying physical behaviour.
This domain of science started in the 1950s with the invention of the first hypervelocity light gas gun at the New Mexico Institute of Mining and Technology [4]. The invention replaced solid propellant with a gas of low molecular weight, enabling velocities up to 3.6 km/s. The previously used guns have used solid propellant, which has expanded all its energy at velocities below 2.5km/s. The invention has proven to be crucial for military applications, and subsequently, it has been under a military embargo for the next decade. The maximum velocity of available guns has been displayed in Figure 3.1

The major work in the field of experimental research is the publication of Piekutwoski [6]. This is the most complete list of publicly available experimental data. With the use of flash radiography, the behaviour of the debris cloud was captured. Three main features of the cloud were highlighted in numerous experiments. This terminology will be used in the following chapters. The first object that is formed is the ejecta veil. Those particles are directed to the outside of the surface. Then the plate gets pierced through and the debris cloud behind the plate is formed. This occurs during the first 15 µs after the impact. It was determined that the majority of the mass of the debris cloud is concentrated at the centre. Aside from documenting the moment of impact, Piekutowski has examined the impact of the plate thickness and projectile diameter on the penetration capability. [6]

In the two decades after performing this experiment, numerous studies have been conducted to examine the physics of the impact in more detail. The research has been conducted both to see what is the resistance of very thin targets [7] as well as thicker targets [8]. The influence of irregular projectile shapes was also examined, as the majority of tests are conducted with spherical or cylindrical impactors. It was observed that irregular shapes have a bigger penetration capability than equivalent spherical projectiles [9].

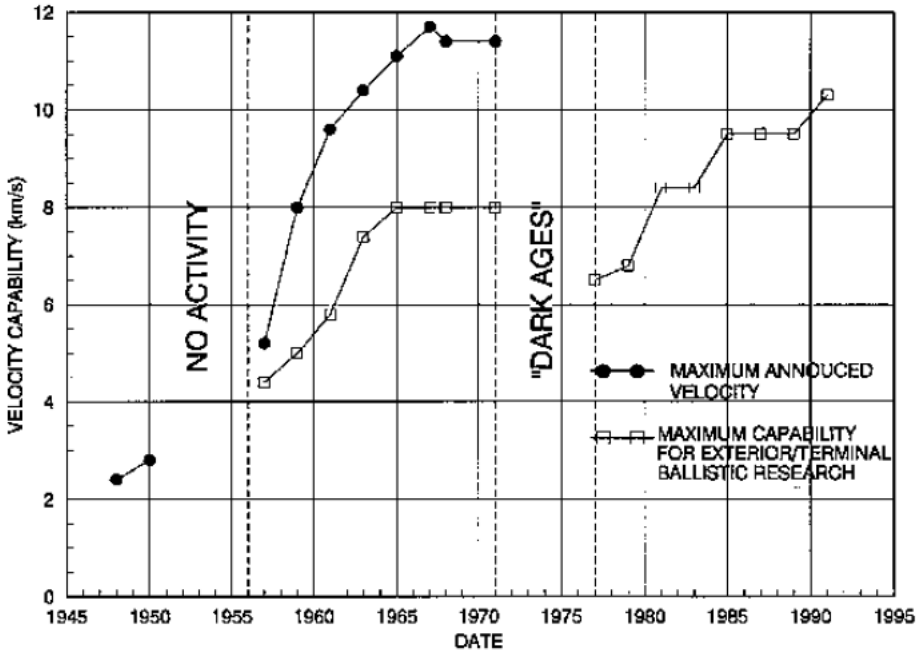

Figure 3.1: Graph indicating the achievable projectile velocities during experiments from 1948 til 1995 [5]

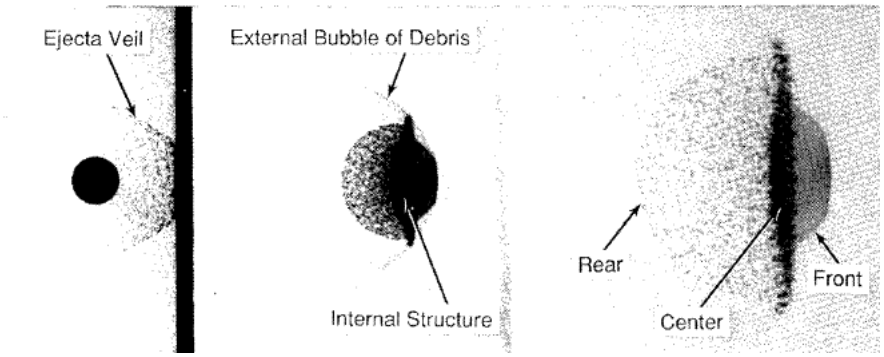

Figure 3.2: Naming convention of the debris cloud phenomena. Note, that on the left the picture of the projectile and ejecta veil is a double exposure. [6]

The development of better gun systems allowed for experimentation with impacts of even higher velocity [10]. Guns are used to test the behaviour of novel materials such as ultra-high molecular weight polyethene [11] nanotube reinforced composites [12] or other composites [13] [14] [15] [16] [17]. Currently, most researchers use a combination of experimental and numerical methods as they complement each other.

3.2. Semi-Empirical

The experimental and numerical approaches enable a detailed investigation of the issue. In practice, however, the obtained data is often used using semi-empirical methods. Those techniques compile data from many experiments and simulations to derive curves that can describe the phenomena in an approximate manner. Therefore, information on the levels of danger can be obtained much easier and faster.

Evaluation of the danger levels posing by a given threat is crucial when a decision has to be made on evasive manoeuvres. In those cases, the system has to asses the threat level quickly. Those systems are also used for the design of the spacecraft, as the cheap semi-analytical method enables extensive iterations without considerable computational burden.

The most common form of semi-analytical technique is Ballistic Limit Equation (BLE), which compiles data from many experiments to create a curve above which the shielding is penetrated and the spacecraft destroyed. The detailed inputs and outputs depend on the model used. The most important models using BLEs available in the literature are highlighted in the next paragraphs.

One of the most popular benchmarks used for predicting spacecraft damage is the NASA standard breakup model (SBM). Thanks to early adoption by NASA and simplicity, it is widely used across the industry today [18]. The most important input parameters for this system are the mass, specific length and velocity profile [19]. Based on the kinetic energy of the projectile divided by the target's mass, the system categorizes impacts as catastrophic or non-catastrophic. The cut-off point is the energy-to-target mass ratio of $40J/g$ [20]. This number is widely used in the industry to classify unsurvivable impacts. As the SBM is a relatively crude measure with binary output, other tools were developed to enable higher fidelity in prediction. This requires more information about the spacecraft as input.

IMPACT smoothens out binary output into a more gradual curve starting at $10J/g$, accounting for incomplete fragmentation [21]. Moreover, it divides the spacecraft into boosters and satellites, due to the much lesser packing density of boosters. Moreover, it uses a few additional inputs such as materials present in the objects to give a better estimate of the damage [22] and debris cloud generation [23].

Particle Impact Risk and Vulnerability Analysis Tool (PIRAT) uses a simplified model of the spacecraft and is optimized for unmanned missions [24]. It uses a three-wall Whipple shield BLE as the components at the inside of the double-wall hull usually have their own casing [25].

Collision Simulation Tool (CST) requires a macroscopic model of the spacecraft, featuring its major components connected by structural links as seen in Figure 3.3. This comes with the inherent benefit when evaluating glancing blows. To calculate the progression of satellite damage, discrete element simulation is used. Dissipation of energy across elements and structural links is considered. When compared to other models, it exhibits outstanding accuracy at the cost of detailed input model requirement [26]. The comparison of accuracy can be observed in Figure 3.4. A more detailed examination of the semi-empirical method is outside of the scope of this review.

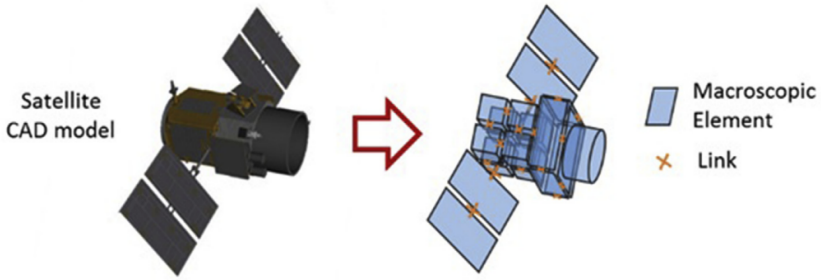

Figure 3.3: Division of spacecraft into macroscopic elements used in CST [27]

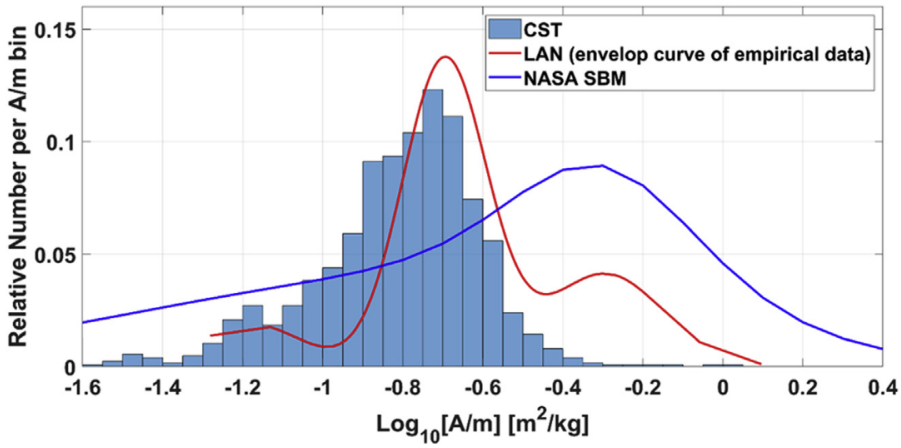

Figure 3.4: Correlation between real-life data, CST and SBM simulations [27]

3.3. Numerical

Numerical methods have seen dramatic raise in significance over the last decades. The computational power available is bigger than ever before. Moreover, techniques used to simulate dynamic behaviour have been developed to a significant extent. This enabled simulation of hypervelocity impacts with much better accuracy.
The hypervelocity impact is a difficult event to simulate. There are many components that lead to this difficulty. Short timeframes, extraordinary pressures and temperature raise. An extreme state at the time of impact leads to the melting and vaporisation of the material at the zone of impact, further complicating the problem. sd

The development of numerical techniques evolved to a much bigger extent than its experimental counterparts. Available computational power has increased dramatically in the last decades. Sophisticated simulation codes were developed that were more efficient and accurate.

In the early days of code development, numerous different techniques were used to overcome the challenges of hypervelocity impacts. The traditional methods such as finite elements used for less dynamic events were insufficient, as they couldn't cope with excessive deformation of the mesh. On the other hand, the particle-based methods were unstable. A combination of those was used in the Particle-in-cell technique [28], in order to overcome the limitations of each approach respectively. That enabled creation a model that can cope with the difficult circumstances of such events. The technique combined the fixed mesh with moving particles that contained all mass of the model. The density of each cell was determined by the number of particles in them. The simulation followed a three-step-cycle in each timestep:

1. Cell momentum and energy computation

2. Advection - the movement of particles across the cells
3. Repartiation of energy and momentum carried by particles into new cells

This solution allowed for limited accuracy but a relatively stable simulation of impacts. Numerous improvements were created such as massless tracer particles to improve the accuracy of the method. However, in the 1990s such software was still insufficient for practical use and the majority of the data was collected using experiments. The true breakthrough was invented when Smoothed-Particle Method was published by Gingold and Mohagan [29] and then applied to such problems a few years later.

3.4. SPH

Smoothed-Particle Method is a meshless technique initially developed for simulation of the complex astrological events. At the time, modelling non-symmetrical events were not possible due to the exponential rise of computational power required without spherical symmetry. Therefore, the modelling of two-star systems or the formation of a star was beyond the capability at the time. The SPH technique was developed as a method to overcome this limitation with the use of inherent properties of meshless method[29].
It uses Newtonian particles that move according to pressure gradient and body forces. The interaction between particles is based on statistics and probability [30], instead of classical contact. This enables much more efficient computation and higher stability when compared to the analysis of each particle-to-particle contact separately. [31]

When the fluid elements have the same mass, the number of particles per unit volume is proportional to the density of the unit. The position of the elements is assumed to be random within the unit due to the complex motion of fluid in the domain. Therefore, determining the density of the unit volume from known distributions of the elements is similar to recovering the probability distribution of a sample.

Statistical smoothing is used to obtain local material information. It gives reasonable estimates of integrals in fewer steps than the standard finite difference method. Two techniques that can be used for statistical estimation are the smoothing kernel method and the delta spline technique. The original paper used the Smoothing Kernel Method, which is also the origin of the technique's name, Smoothed Particle Hydrodynamics. The smoothing kernel function dictates the area in which each particle interacts with its neighbour, as shown in Figure 3.5.

It is robust and enables the use of a high number of degrees of freedom. It has quickly gained popularity in the academic community and a lot of applications have been found since, but the method is not without limits. The first difficulty is boundary conditions. As the objects lack clearly defined boundaries, additional steps are commonly used to allow for the proper application of boundaries. A common way is the creation of ghost massless nodes that are fixed and can interface with surrounding particles with no movement. This reduces the accuracy of the simulation when a precise boundary is required.
The second difficulty is tensile instability, which tends to lead to particle clumping under heavy tensile loading. It is well-known problem since the invention of the technique. It necessitates the use of artificial viscosity to damped this behaviour [3]. Recently, a study was published by Wen and Chen [32] which looked at the effects of aluminium spheres on thin Al plates, similar to the research conducted by Piekutowski a decade earlier. The research work represents one of the most detailed descriptions of the failure evolution to date.
The behaviours and reactions that happen at specific impact velocities and energies can vary. This issue was explored in a recent publication by Signetti and Heine [33], which highlights the significance of experimental data in determining material properties and coefficients for simulation. This is particularly vital when taking thermal effects into account, as these can be highly influenced by input parameters. Given the difficulty in obtaining such data, modelling thermal effects is avoided when possible. A comprehensive summary of different ways that the SPH technique was used in recent research can be found in the work from Meng et al. [3].

3.5. Theory behind SPH

The SPH technique utilizes a collection of dispersed particles to represent a specific area of interest. Using these particles, approximations of the field functions and their derivatives are created. To determine the particle approximation of a continuous field function, $u(x)$, a kernel approximation of the field function is established in the following form:

$$u(\boldsymbol{x}) = \int_{\Omega} u\left(\boldsymbol{x}'\right) W\left(\boldsymbol{x} - \boldsymbol{x}', h\right) d\boldsymbol{x}' \tag{3.1}$$

where W is the smoothing function that is required to satisfy series of conditions [34] and Ω is a non-zero region of the smoothing function called smoothing domain. The smoothing function used in this research is the B-spline function, which is the most commonly used solution[35].

$$W\left(\boldsymbol{x} - \boldsymbol{x}', h\right) = \frac{C}{h^d} \times \begin{cases} 1 - \frac{3}{2}\xi^2 + \frac{3\xi^3}{4}, & 0 \leq \xi < 1 \\ \frac{1}{4}(2-\xi)^3, & 1 \leq \xi < 2 \\ 0, & \xi \geq 2 \end{cases}, \tag{3.2}$$

where h is the smoothing length, C is a constant depending on space dimensions, d is the number of space dimensions, $\xi = r/h$ and $r = |\boldsymbol{x} - \boldsymbol{x'}|$ is the distance between particles $\boldsymbol{x}$ and $\boldsymbol{x'}$.

By replacing the continuous integral over a specific region Ω in Equation 3.1 with a summation of neighbouring particles at a certain point, the kernel approximation is discretized. This results in a particle approximation of the field function. The continuous form of the approximation becomes a sum of the particles in the vicinity. Specifically, for particle i located at x_i, the approximation of the field function can be represented in the following manner:

$$u\left(\boldsymbol{x}_i\right) = \sum_{j=1}^{N} \frac{m_j}{\rho_j} u\left(\boldsymbol{x}_j\right) W\left(\boldsymbol{x}_i - \boldsymbol{x}_j, h\right) \tag{3.3}$$

where N is the total number of particles within the influence area of the particle at $\boldsymbol{x}$. The number of particles that are included in the computation is determined by the smoothing length, h, multiplied by a scalar constant κ. This cut-off distance defines the support domain of the smoothing function. The m_j is the mass and ρ_j is the density. This method of summing over nearby particles is known as particle approximation, and it states that the value of a function at a specific particle can be estimated by taking the average of the function's values at all particles within the support domain and weighting each by the smoothing function [36]. The governing equations are discretized based on particles, and this in turn is used to calculate the local density, velocity, and acceleration of the material. The procedure of summation over the neighbouring particles is referred to as particle approximation, which states that the value of a function at a particle can be approximated by using the average of the values of the function at all the particles in the support domain weighted by the smoothing function. The same procedure can be performed with the derivative of the function. The graphical representation of the effect of the particle on surrounding volume due to smoothing is presented in Figure 3.5

$$\langle \nabla \cdot u(\boldsymbol{x}) \rangle = -\sum_{j=1}^{N} \frac{m_j}{\rho_j} u\left(\boldsymbol{x}_j\right) \cdot \nabla W\left(\boldsymbol{x} - \boldsymbol{x}_j, h\right), \tag{3.4}$$

The Equation 3.4 shows that the gradient of a function at a specific particle located at x can be approximated by using the summation of the function's values at all particles within the support domain. These values are weighted by the gradient of the smoothing function. This process of using summations to approximate the integral is known as the particle approximation, which is the fundamental aspect of the SPH method, allowing for a simple and accurate solution without the need for a background mesh [34] [36].

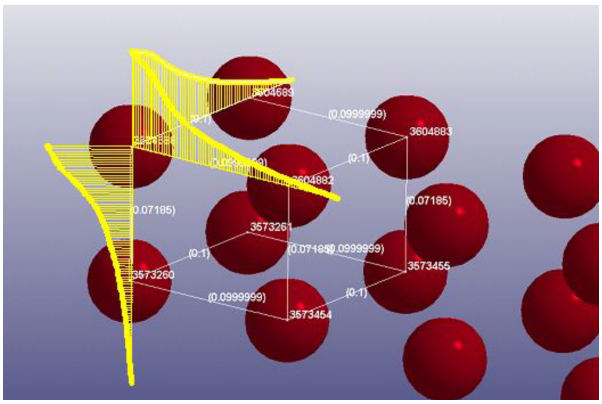

Figure 3.5: Graphical representation of the SPH [14]. The yellow plot describes the smoothing function that dissipates from the centre

4

Replication of Previous Studies

This chapter describes the replication of previous studies related to hypervelocity impact simulation. The research presented in this chapter aims to reproduce the results of previously published studies, using LS-DYNA, a widely used explicit finite element software well-suited for simulating high-speed impact events. The primary goal of this part of the research is the development of the simulation methodology and validation using the experimental and numerical data from the original studies. The validation process involves a comparison of key outputs, such as the diameter of the damage zone and the stress field, to the corresponding experimental data. This chapter provides a description of the simulation approach, the experimental setup, and the validation process, along with the results of the replication and validation studies. Two studies are chosen to be replicated among the documentation collected in the literature review, based on following criteria:

- Recency - As the technology progresses, research papers can present more accurate data than before. Moreover, the focus of the research changes, as more advanced topics are founded in the earlier works. Using recent papers enhances the applicability of reproduced research to the current topic.
- Combination of experimental and numerical results - The chosen paper must have both experimental and numerical components. The experimental basis is essential to understand the true behaviour of the system, but the numerical component is necessary for replication. Without it, the simulation could diverge from the experiment, without clear reason. Comparing new simulations with validated numerical work in the reference is the preferred option.
- Availability of model inputs - To properly replicate the study, numerous inputs have to be described. This includes the geometrical set-up of the experiment, impact velocity, material and experimental conditions. Moreover, as the numerical study is considered, the material model and equation of state parameters are crucial and enable close matching results. The use of a combined experimental and numerical study as the reference has the benefit of making such data available.
- Availability of detailed output - The output gathered in the study has to be replicable and given sufficient detail to determine whether the results of the replication are successful. Moreover, the measured criteria shall be similar to the ones that are used in the following stages of the research. The number of data points gathered in the study is another variable that needs to be examined, as a bigger dataset could be beneficial during the replication process.
- Relevance - The study has to be performed using comparable technology to the one used for the thesis. Moreover, the experiments should be as close as possible to those that were performed by ESA. That includes materials, impact velocity and the focus on the study itself.

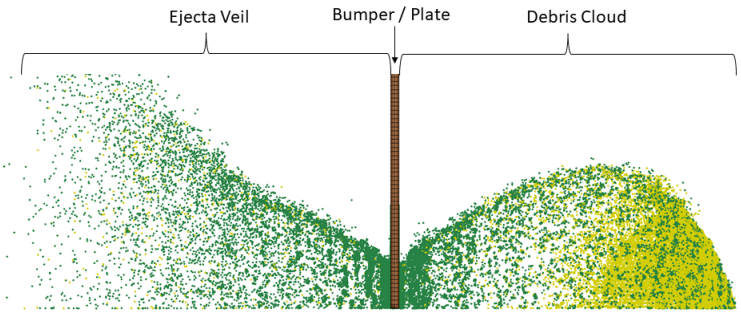

Figure 4.1: Side view of the simulated impact into a single plate term with a description of terms used in the rest of the work. Half of the impact zone is pictured, due to the used symmetry condition.

4.1. Replication of study by Legaud et al.

The study from Legaud, Le Garrec, van Dorsselaer and Lapoujade has been determined to be the best match of the above criteria. It is titled 'Improvement of satellites shielding under high-velocity impact using advanced SPH method' and was published in 2019 at the 12th European LS-Dyna Conference [37]. It combines comprehensive numerical study with experimental data from work performed by Sibeaud et al. [38].
The study conducts sensitivity analysis for parameters, judging the influence of more computationally expensive options on the accuracy and performance. The parameters examined are:

- Number of particles in plate thickness
- SPH formulation
- Pressure cut-off

The measured data includes geometrical dimensions of the debris cloud at various times after impact, combined with the velocity at the peak of the debris cloud. It also contains the measured crater diameter, which is especially relevant for the research, as it is in alignment with what is tested in work by ESA. Moreover, the paper provides a detailed description of the model inputs and outputs, compared with the experiments. The depth of detail is unique when compared with similar works.

The second study has been chosen for its description of the stress field around the impact location and is described in more detail in section 4.2.

4.1.1. Background and Methodology

The study examines a singular plate impacted by a spherical projectile at 5.941 km/s. Both the bumper plate and the projectile are made out of aluminium. The impact occurs at the normal angle and the data collected is related to the debris cloud parameters as well as the crater formed in the plate itself. The definition of those terms is displayed in Figure 4.1 The formed debris cloud and its parameters are presented Table 4.1 and the resulting values are shown in Table 4.2. Cloud diameter, length and velocity at the peak velocity are measured. Additionally, the crater size is examined. Those parameters provide valuable information for the remaining part of the work because the accuracy of the debris cloud is essential for further work on the double-plate system. As the second plate is impacted by the cloud, its numerical representation shall be close to the experiments. The experimental setup and output measurements are pictured in Figure 4.2.

As a first step of the replication, a simplified model was created. Its goal was to check whether the material model and equation of state worked as intended. The simulated experiment in the original paper comes from Sibeaud et al. [38]. In this experiment, impact tests were performed at 0°angle using various projectiles. The simulation focuses on the third configuration of the experiment, which had details indicated in the Table 4.1. In the experiment, the aluminium sphere impacts the singular aluminium plate at 5.941 km/s at the normal angle. The impact is recorded using a high-speed data acquisition system. The results of the impact are examined at 16 µs after the initial contact. Some

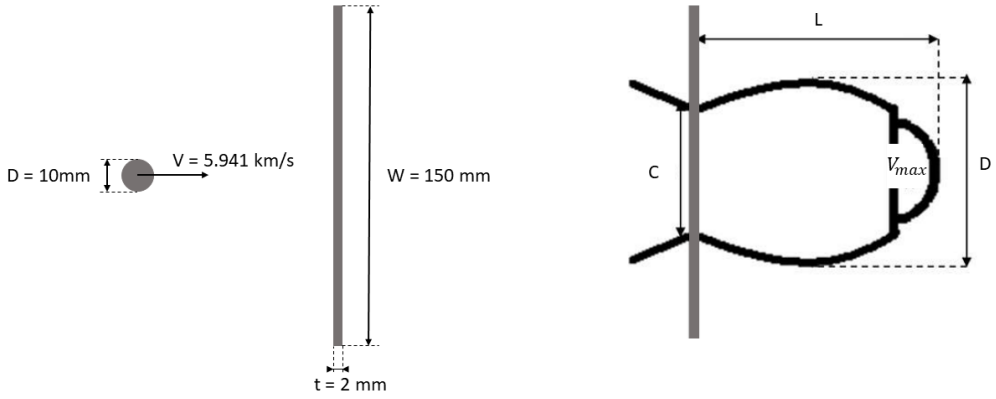

Figure 4.2: Representation of experiment setup (left) and measured parameters of the debris cloud (right) in the original experiment [37]. Measured values of parameters are presented in Table 4.2

Name	Value
Projectile diameter	10mm
Projectile velocity	5.941 km/s
Impacted plate dimensions	150mmx150mmx2mm
Impacted plate material	Al 6061-T6

Table 4.1: Parameters of the experiment that has been used as a reference [38]

studies prefer to examine the final state of the crater, rather than one that is still forming. However, the reference study only examines the impact zone at 16 µs, disregarding the final state of the plate. As the measurement of the crater is done after the experiment is concluded, the measurement in the simulation should be done after a sufficiently long time after the impact. The short timeframe of 16 µs does not allow for the full formation of the crater. For further simulations, the termination time is extended to ensure that the final diameter is achieved. The material model and equation of state used in the simulation have been exhaustively described in the study. The Steinberg-Guinan material model has been described in Table 4.3. As this material model had resulted in insufficient accuracy, the Johnson-Cook model was also used for comparison. Input parameters of this model are given in Table 4.5 The EOS parameters are presented in Table 4.4.

During the replication process, three models have been used with increasing complexity and computational cost. All were quarter-models, like in the original study and pictured in Figure 4.3. Due to the sensitivity of results on the symmetry condition settings, other simulations in this work have been conducted without the use of symmetry. However, as precise coordinates of the symmetry plane were given in this work, two symmetry conditions are used which allows for the use of quarter models. The consequences of symmetry condition is further discussed in subsection 4.1.3. All models have used the tied boundary condition at the outside perimeter. Considering the use of planes of symmetry, the fixed boundaries were applied on two walls opposing the symmetry planes. Three different models of ascending complexity were created in order to replicate the study. The mesh settings of each model are described in Table 4.6. The first model has been devised at a very low particle count in order to enable rapid processing of a local computer. Therefore, the SPH packing density is much lower than in the original. Moreover, the SPH plate has been constrained directly by a fixed boundary, without a finite element zone. The model has been used for rapid experimentation and is not able to accurately picture the complex debris cloud due to an insufficient amount of particles.

Measures	Parameters	Experiment results (16µs)
Cloud maximal diameter	D	65.6 mm
Debris cloud length	L	81.1 mm
Crater diameter	C	18.9 mm
Debris velocity at the cloud front	Vmax	5.296 km/s

Table 4.2: Results of the experiments performed by Sibeaud et al. [38]. The aim of the simulation is to achieve close matching to those results

Parameter	Value	Parameter	Value
Density (g/cm3)	2.703	Constant parameter b' factor	6.52
Shear modulus (Mbar)	0.276	Constant parameter h factor	-0.000616
Initial elastic limit (Mbar)	0.0029	Atomic mass	26.98
β factor	125	Melting temperature (K)	1220
Exponent n	0.1	a factor	1.5
Melting elastic limit	0.0068	Pressure cut-off (Mbar)	0.02
B factor	6.52		

Table 4.3: Steinberg-Guinan material model input parameters

The 2nd model improved packing density in the plate while maintaining reduced particle count. A portion of the central SPH was modelled with the same spacing as the original, leading to similar debris cloud behaviour after impact. In this case, the fixed boundary condition was also applied to two edges of the SPH zone. Due to its small size, the fixed boundary condition was relatively close to the impact zone. This is undesirable, as it influenced the forming of the crater diameter, by artificially stiffening the structure.
The final model corrects this issue using a larger SPH zone as well as a Finite element area around it. This model fully matches the original mesh in both the number of particles and FE. It is more computationally demanding than two prior iterations but enables true replication of the simulation conducted in the original study. The model uses tied node-to-segment contact between particles and finite elements. The boundary condition is applied to the nodes at the outside perimeter of the finite elements. This mesh can be observed in Figure 4.4 and is used for obtaining the final replication results.

4.1.2. Results of the Replication

The general behaviour of the new model matches the figures provided in the original study, as observed in Figure 4.7. A debris cloud is formed in the same shape and at an equal rate as in the original. The damage propagation is presented in Figure 4.8 The ejecta veil is clearly defined and forms rapidly upon first contact. Following, a debris cloud is formed. Due to its spherical nature, it is often called a bubble. A significant portion of the mass at the centre and front of the debris cloud consists of the projectile surrounded by the layer of debris from the plate. This is expected behaviour - depending on impact conditions, there might be a bigger fragment of the projectile still intact.

Parameter	Value
C	0.524
S1	1.4
S2	0
S3	0
Gruneisen parameter γ	1.97
A factor	0.48
Initial internal energy (10^e5J)	0
Initial relative volume	0

Table 4.4: Gruneisen EOS parameters [37]

	Al 2024-T3
Publication	Lacome et al. [39]
Density [g/cm3]	2.785
Shear modulus [Mbar]	0.286
A [Mbar]	0.00265
B [Mbar]	0.00426
c [-]	0.015
n [-]	0.34
m [-]	1
Specific heat $[10^7 \frac{Ncm}{gK}]$	0.875e-5
Melt température [K]	775
Room temperature [K]	273

Table 4.5: Johnson-Cook Material model parameters used for the replication [40]

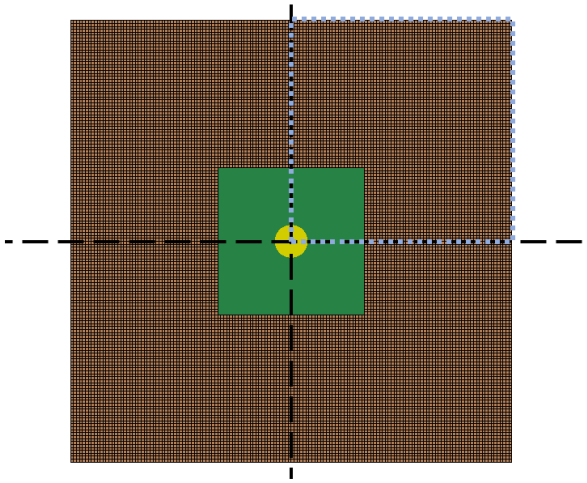

Figure 4.3: Display of the symmetry planes used as black dashed lines. Using the symmetry, only a quarter of the model is simulated in the replication of Legaud et al. [37]. The quarter model is highlighted in blue.

The propagation of the debris cloud continues smoothly and without any discontinuities or erroneous particles.
The velocity measurement is conducted on the first 10% of the volume of the particles of the debris cloud, as shown in Figure 4.2. This enables capturing the true velocity of the cloud, rather than the individual particle. If only the peak speed of the particle is used, the method would be prone to error in case a local anomaly is present, for example, due to tensile instability. As in the experiment, the axial velocity is measured instead of the total velocity. This eliminates the radial component, as the sensors used in the experiments measure axial velocity only.
The surrounding FE plate undergoes minimal deformation, due to clean penetration in the SPH zone. As seen in Figure 4.5, the cloud properties of the replication using Johnson Cook material are within 1% of the experiment, which is in a similar range as the source simulation.

The simulation has been replicated closely to the original, using original parameters described in subsection 4.1.1 with the exception of the material model. The Johnson-Cook material model from Lacome et al. [39] has proven to be a superior choice when compared to the original Steinberg-Guinan equations, as pictured in Table 4.8. Better accuracy with the use of the Johnson-Cook model is supported by its bigger presence in the hypervelocity research [33]. The most drastic improvement was observed in the hole diameter measurement as can be observed in Figure 4.6. The use of the original material model led to over 25% error, whereas the Johnson-Cook achieves below 1% error. The cloud parameter results are pictured in Figure 4.5 and the tabulated values are given in Table 4.8. The Johnson-Cook material model used to achieve those results [39] is described in more detail in section 5.4. For those tests, all other parameters such as mesh size were kept constant.

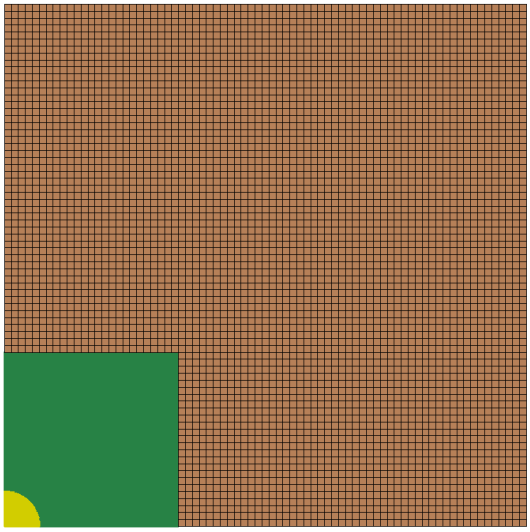

Figure 4.4: Display of the final mesh of the quarter-model used in the simulation. 707024 SPH particles are used and 10000 Finite Elements. The quarter of the ball is presented (yellow) that impacts the SPH impact zone of the bumper (green). The SPH zone is surrounded by Finite Elements (brown).

Model Iteration	Part	Dimensions of SPH zone [mm]	Number of SPH particles in principal directions	Total number of SPH particles in the part
1st	Plate Sphere	37.5 x 37.5 x 2 D = 10	50 x 50 x 10 10 x 5 x 5	25 000 138
2nd	Plate Sphere	12.5 x 12.5 x 2 D = 10	100 x 100 x 16 80x80x40	160 000 67 024
3rd	Plate Sphere	25 x 25 x 2 D = 10	200 x 200 x 16 80x40x40	640 000 67 024

Table 4.6: Settings of the mesh used for three iterations of the mesh.

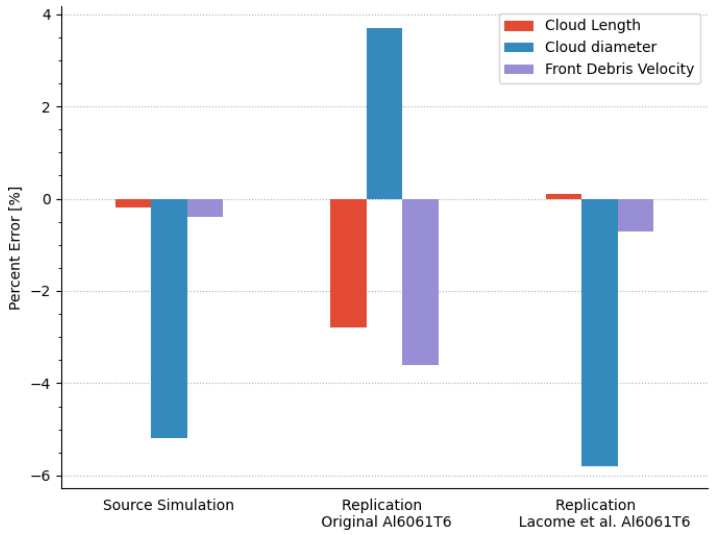

Figure 4.5: Percentage error of three measured parameters of the debris cloud with respect to the experimental value. Cloud length, diameter and the velocity of the front of the debris cloud are compared. Replication using the material model given in the original paper has much higher error than one using a material model from Lacome et al. [39]

No.	Change	Result
1	Modified SPH formulation from 5 to 0	No difference
2	Increased Cut-Off Pressure by a factor of 10	
3	Increased SPH contact distance	
4	Timestep for High-Explosive Simulation was used	
5	Used Linear Polynomial EOS	Crash
6	Used Gruneisen EOS with constant C multiplied by 1000	
7	Used Johnson Cook Material Model From Lacome et al.	Improved result

Table 4.7: Results of different changes implemented to test the model

	Material Model	Hole Diameter [mm]	Front Debris velocity [km/s]	Cloud length [mm]	Cloud diameter [mm]
Experiment	-	18.9	5296	81.1	65.6
Ref. Simulation	Original	18.4	5316	81.3	69
Difference	-	2.6%	-0.4%	-0.2%	-5.2%
Replication 1	Original	24	5489	83.4	68
Difference	-	-27.0%	-3.6%	-2.8%	-3.7%
Replication 2	Lacome et al.	18.8	5334	81	69.4
Difference	-	0.5%	-0.7%	0.1%	-5.8%

Table 4.8: Results of the replication of work from Legaud et al. [37]. The difference between the two replications is the source of the material model.

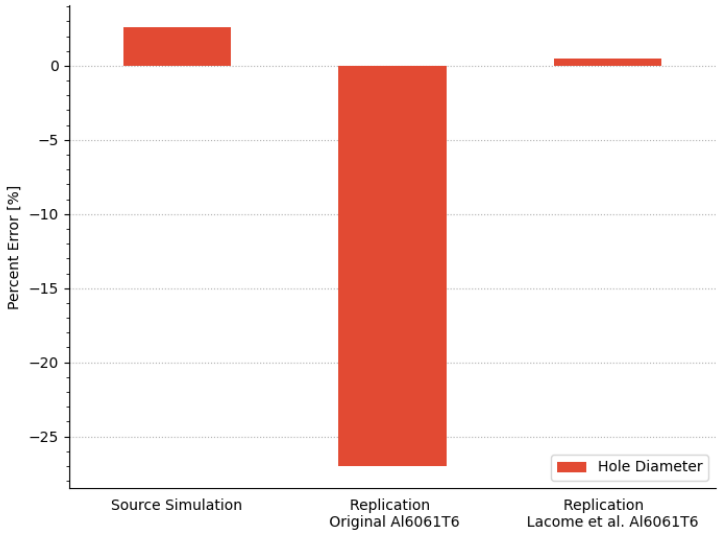

Figure 4.6: Percentage error of the damage zone diameter, compared to the experimental value. The material model given in the original paper produces much higher error than the material model from Lacome et al. [39]

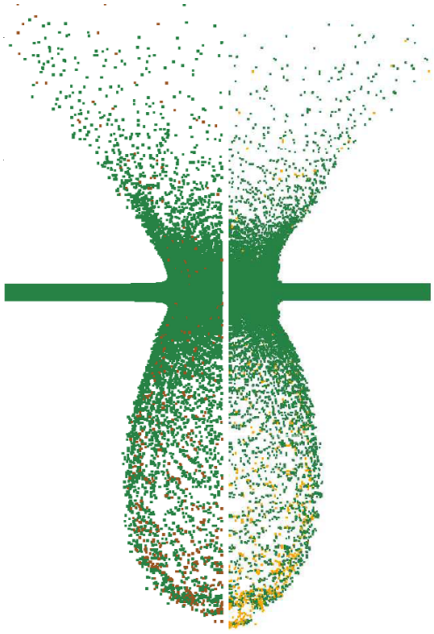

Figure 4.7: Comparison between debris cloud from the replication (left) and the original study (right) at 10µs after impact

.

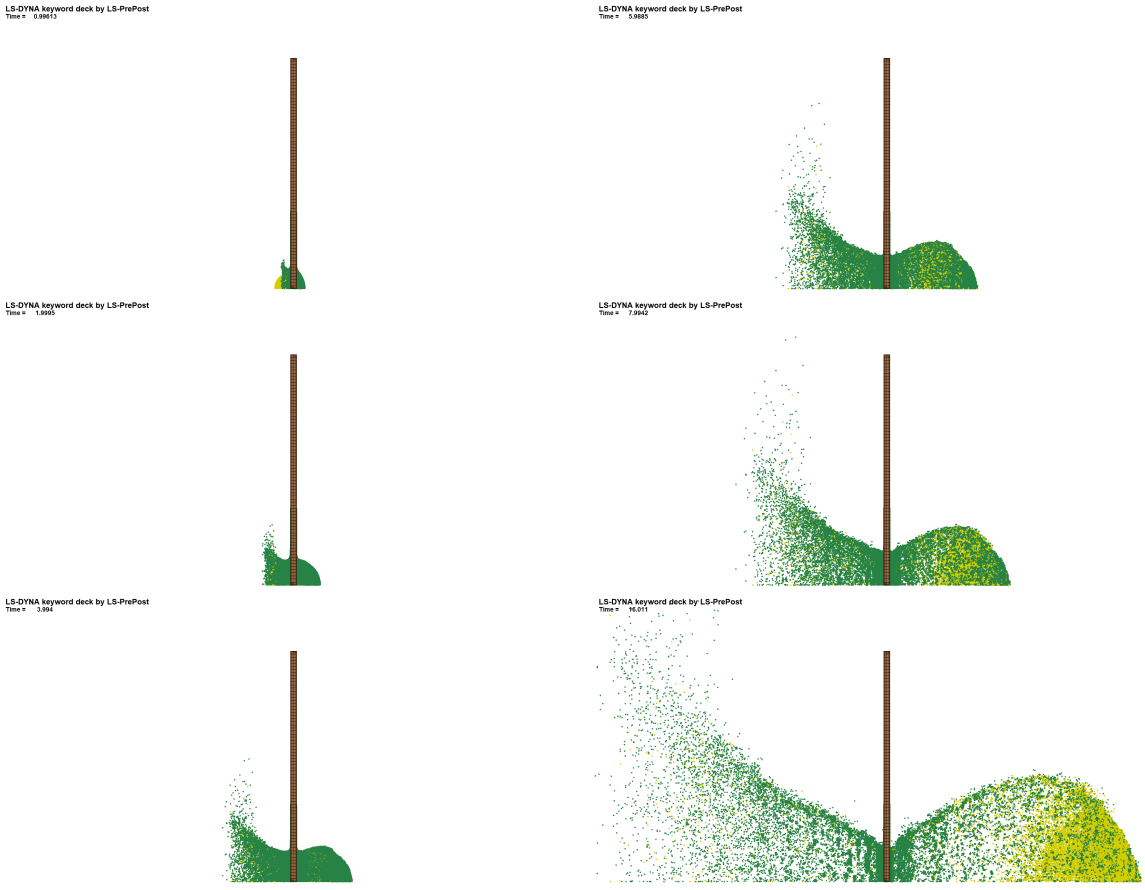

Figure 4.8: Progression of damage in the replicated model. The evolution of debris cloud in the first 16 µis displayed. The simulation used the Johnson-Cook Material model [39].

4.1.3. Analysis and Discussion

The model has performed successfully and a very close match to the original was achieved. However, a series of iterations were required to achieve the desired result. Most importantly, the Johnson-Cook material model was used as it allowed for the closest matching to the experiments and original simulation. Other parameters used were following the instructions given in the paper. The Steinberg-Guinan equations have performed below expectation, especially when the final crater diameter was considered. This is best observed in the error diagrams featuring the offset from an experiment in Figure 4.5 and Figure 4.6. The original material model, which is Steinberg-Guinan has achieved a weak correlation with the original simulation and experiments. On the other hand, the simulations made with Johnson Cook Model from Lacome et al. [39] achieved comparable accuracy to the original work.

In the initial model of the hypervelocity impact simulation, identifying the subset of particles that formed the front of the debris cloud posed a challenge. There was no clear definition of this term, and it was not immediately clear how to identify these particles in the simulation.

Upon further examination, it was discovered that the front of the debris cloud was actually composed of particles that had undergone spalling and tensile instability. These particles had significantly higher velocities than the rest of the debris cloud and were often formed from the subset of SPH particles that experienced these phenomena. This initial formation is pictured in Figure 4.9.

It was also found that the presence of the symmetry boundary condition in the initial model contributed to the occurrence of tensile instability. That is due to the interaction of the boundary condition with the neighbouring particles. During impact, an incorrectly placed boundary leads to the additional tensile strain of the particles. That leads to clumping and so-called tensile instability, which is to be avoided. It is recommended that the symmetry plane be placed at a distance of half the specific length of the SPH particles in the structure. In this case, with a specific length of 0.125mm, the symmetry plane should have been placed at 0.0625mm from the simulated structure. However, the recommended distance was doubled, placing it wrongly at 0.125mm away from the structure. This has led to the problem described above. By using the recommended spacing distance, It was possible to eliminate this problem and more accurately define the front of the debris cloud as the first 10% of the volume of the cloud, starting from the particles that formed a clearly shaped bubble at the front.

The progressive formation of the debris cloud is shown in Figure 4.10. One of the first features to be formed is the ejecta veil, which is composed largely of material from the plate itself.

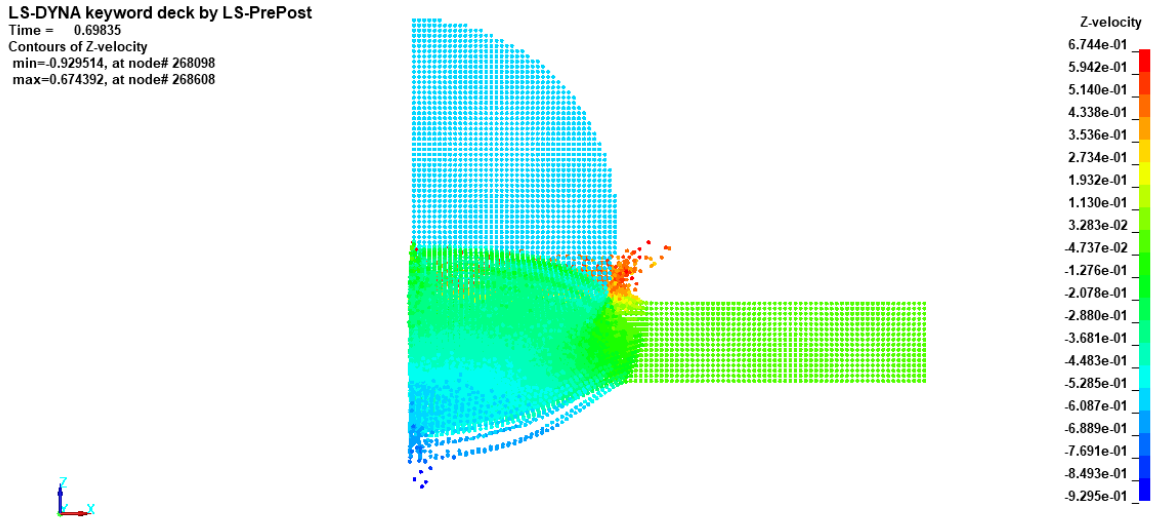

Figure 4.9: Display of tensile instability at the beginning phases of the impact in the reduced model with symmetry plane at the distance two times larger than recommended.

4.2. Replication of Study from Plassard et al.

The second work that has been replicated is the conference paper from Plassard, Mespoulet and Hereil titled 'Hypervelocity impact of the aluminium sphere against aluminium plate: experiment and LS-Dyna

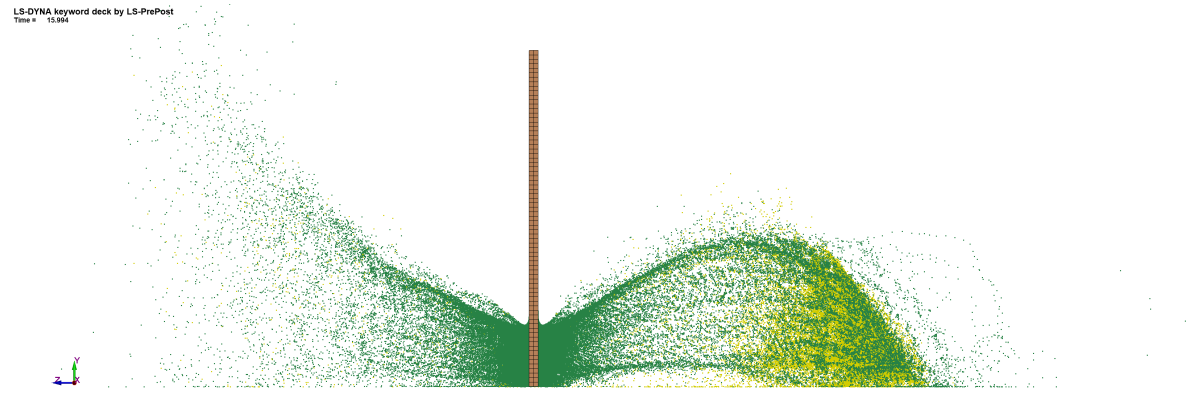

Figure 4.10: The model shows the excessive separation of particles at the front of the debris bubble. This can be reduced by changing the symmetry boundary condition.

correlation'[41]. The study was conducted at Thiot Ingenierie in France. The study examined an impact at 4km/s. The LS-Dyna simulation replicates the experiment performed using a two-stage light gas gun. The aim of the study was to compare the LS-DYNA 3D Simulation with 2D and 3D Multi Material Arbitrary Lagrangian Eulerian Method (MMALE) solvers.

4.2.1. Background and Methodology

In the study, both MMALE and SPH simulations were conducted to replicate the same experiment. However, the MMALE simulation was unable to accurately reproduce the rear plume of the impact, which is important in determining the penetration of Whipple shields. On the other hand, SPH performed much better in this task and is therefore the focus of this replication.
The SPH simulation used 3D-SPH with plane symmetry to model a plate with dimensions 100mm x 100mm, with an SPH zone of 20mm x 20mm. The outside zone was modelled using Finite Elements, with a transition zone using hybrid SPH/FEM elements to improve the accuracy of shock wave transmission across the interface. This transition zone is described in detail in subsection 5.7.1.
The model was created using the framework developed during the replication of the study from the previous chapter. The changed parameters include the geometry, mesh density and different contact definition between finite elements and SPH. The simulation was iterated using different material models, symmetry conditions and mesh density to examine their respective influence on the results.
The original model was simulated using plane symmetry. In the replication, both the full model and half-model were examined as the computational capabilities available were sufficient. Therefore, here the full model is described, with the plane-symmetry model using half as many elements and particles. As described in Table 4.9, the centre zone in the plate contains 409 600 SPH particles with 38400 FEM elements surrounding it. The model uses 16 particles through the thickness, which is recommended value by a study from Legaud et al. [37]. The FE has 4 elements through the thickness, which results in an element aspect ratio of 2. The sphere uses 7208 SPH particles. Therefore, the mesh density of the plate and the sphere is in the same order of magnitude. The final mesh can be observed in Figure 4.11.

	Dimensions of SPH zone [mm]	Number of SPH particles in principal directions	Total number of SPH particles in the part
Plate	20 x 20 x 2	160x160x16	409 600
Sphere	D = 1.5	24 x 24 x 24	7208

Table 4.9: Details of the SPH mesh of the replication.

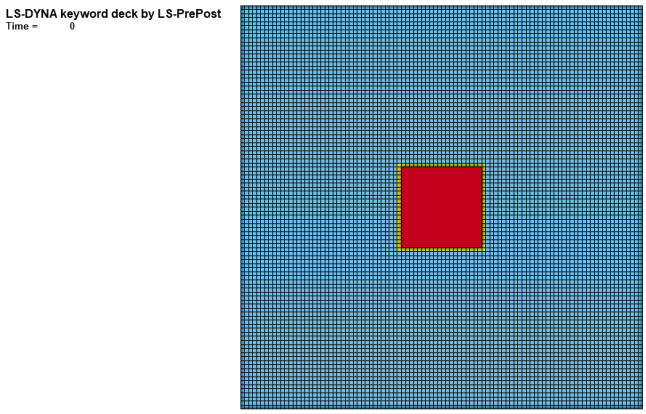

Figure 4.11: Display of the full plate used in replication of study from Plassard et al. [41]

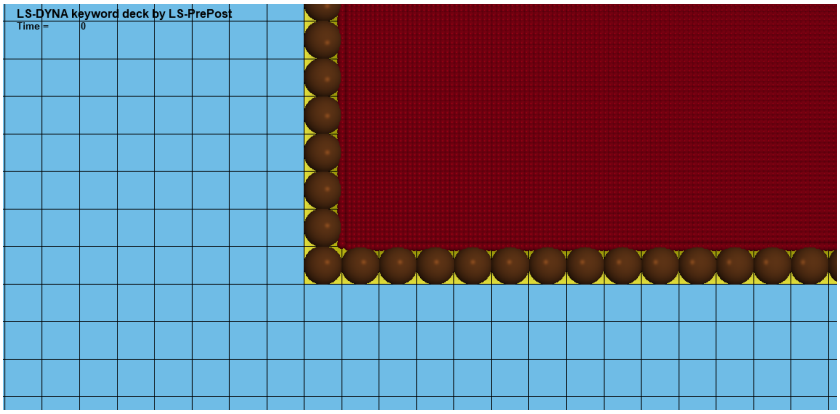

Figure 4.12: Detail of the mesh used in the replication. The SPH particles within the FE are visible, and used for a smoother transition between the SPH and FEM.

The material model and EOS have been taken directly from the study, to ensure the closest correlation. Therefore, the elastic-plastic-hydrodynamic material model was used, given in Table 4.10. This material is not optimal for use in hypervelocity impact, due to its poor debris cloud formation related to particle clumping as shown in Figure 4.16. However, its benefit lies in the small number of input parameters required. As the focus of this work is on the stress field, the material model is deemed acceptable. To accompany it, the Mie-Gruneisen EOS is used, shown in Table 4.11. There were several iterations of different simulation setting to arrive to functional simulations, the main ones are highlighted in chapter 8

	Al 2024
Publication	Plassard et al. [41]
Shear modulus [Mbar]	0.286
Elastic limit [Mbar]	0.0026

Table 4.10: Input parameters for elastic-plastic-hydrodynamic material model

	Al 2024
Publication	Plassard et al. [41]
C	0.5328
S1	1.338
S2	0
S3	0
Gruneisen coefficient γ	2.0
A	0
Initial internal energy $(10^e 5J)$	0
Initial relative volume	0

Table 4.11: Input parameters for Gruneisen EOS

4.2.2. Results of the Replication

The main objective of this replication is to compare the stress field between the reference and the examined model. Von-Mises' stress was used as an indicator as this was available in the published study. In the original, numerical effects on the stress field are visible, caused by the sharp corners of the square SPH zone. The same behaviour can be observed in the replicated model. The peaks and valleys of the stress field are in the same locations, with different minor differences in the size of the peak stress zones. At 3.3 µs after the impact, the wave propagates from the centre beyond the SPH zone, as seen in Figure 4.13. The shape of the zone with higher stress is nearly circular. This shape is distorted with clear peaks and valleys at 6 µs as seen Figure 4.14, which are the result of the connecting zone between FE and SPH. As the SPH zone is square, it leads to non-uniform stress distribution. The wave continues expansion at 8.3 µs which much lower peaks, shown in Figure 4.15.
The simulation has confirmed that the use of the elastic-plastic-hydrodynamic material model is inappropriate when the debris cloud is relevant. That is because the use of this model leads to the clumping of particles and unrealistic debris cloud development, as observed in Figure 4.16. In the picture, insufficient mesh density to describe debris cloud can be seen. As the study focused on the stress field of the single plate, the correct representation of the debris cloud was not the primary focus.

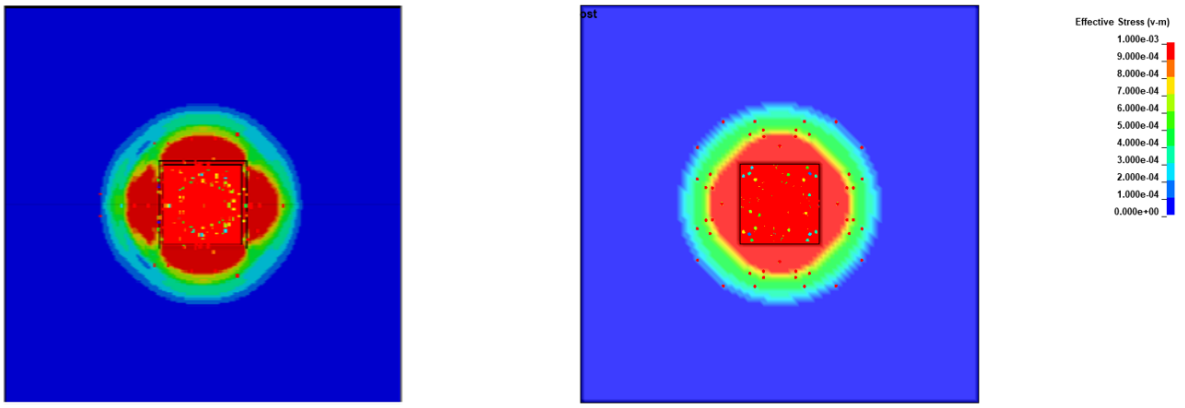

Figure 4.13: Comparison of results between original study (left) and the replication (right) at 3.3 µs after impact.

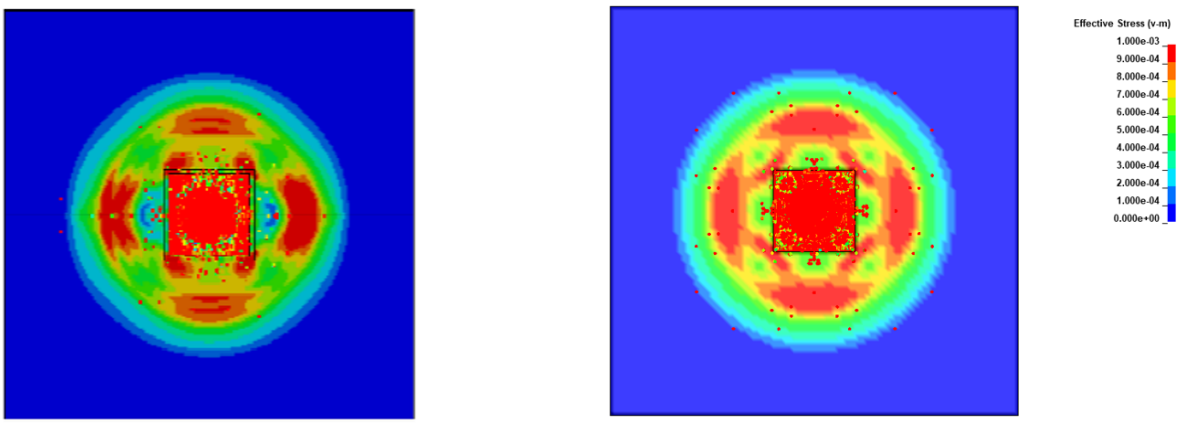

Figure 4.14: Comparison of results between original study (left) and the replication (right) at 6.0 µs after impact

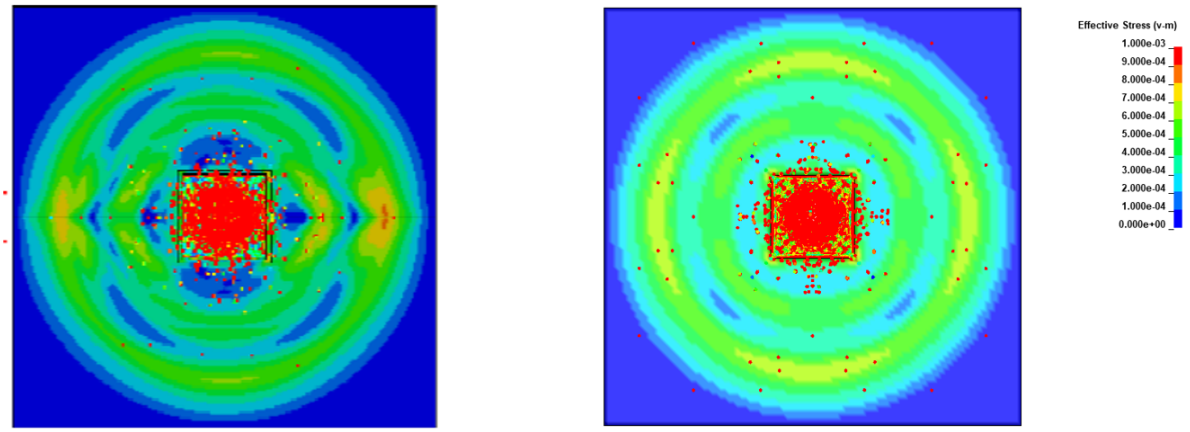

Figure 4.15: Comparison of results between original study (left) and the replication (right) at 8.3 µs after impact

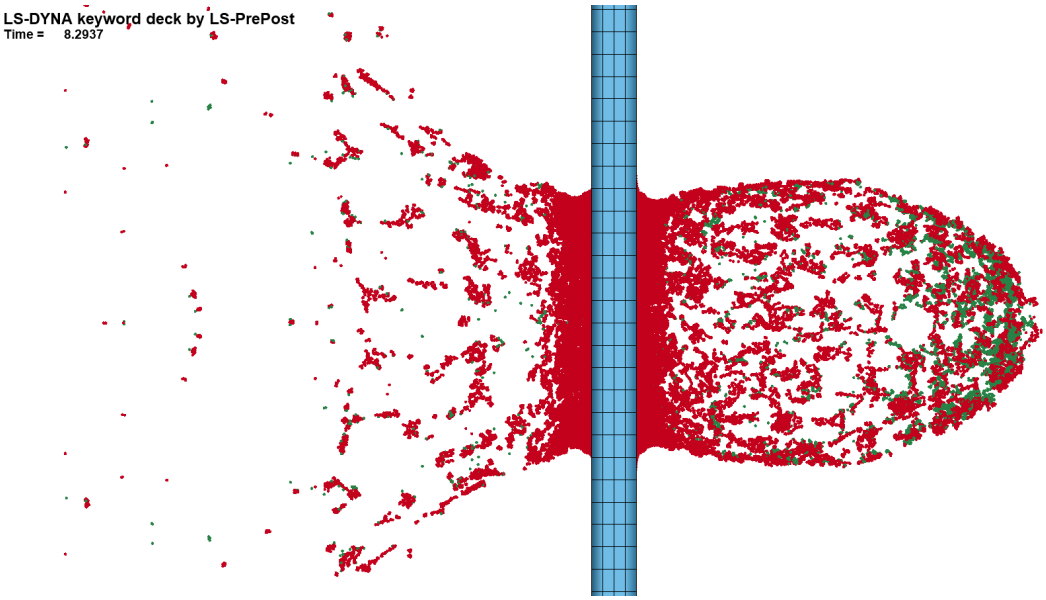

Figure 4.16: Side view of the debris cloud formation during simulation of the impact using the elastic-plastic-hydrodynamic material model. The debris cloud is unrealistic due to the clumping of particles.

4.2.3. Analysis and Discussion

The replication of the study has begun using the inputs given in the paper. However, the list of used parameters was incomplete, therefore some simulation parameters had to be iterated based on the prior knowledge and desired output. In this study, the visual plotting of the stress field is the most important result. The comparison is made with the use of the fringe plots of Von Mises's stress in the plate. The limits of stress are set to be identical to the original, to provide easy visual identification of discrepancies. The plots are captured at the same time as in the original simulation, with a precision of 0.02 µs.

The result of the simulation matches the original in major features of the stress field. Starting from the initial 3.3 µs snapshot in Figure 4.13, the circular stress zone is captured. The high-stress field in the middle is spreading almost uniformly. Due to the connection between SPH to FEM in a square shape, the circular shape is disturbed slightly. In the following picture at 6 µs after the impact in Figure 4.14, the stress field is more complex. The low-stress circular zone has expanded at the speed of sound, but the inner peaks are now located at four positions in the middle of each square wall. This is an artefact of the numerical method used, as the SPH zone is a square inside of a larger FE plate. Both in the original and the replication, a region of higher stress is also seen at the corners of this square. There is a small discrepancy in the shape, as the replications seem to have those features connected, whereas it is less visible in the original. However, the magnitude and the general trend is matching.
In the final picture at 8.3 µs after the impact in Figure 4.15, the stressed zone is more spread out, with peaks at lower magnitudes. The location of the major peaks and valleys in stress is matching, however, the magnitude is slightly higher in the original. This was deemed acceptable as some parameters were undisclosed in the study. Moreover, the used version of LS-DYNA is considerably different, due to the age of the study, which was published over 10 years earlier.

5

Methodology

This chapter presents the methodologies and models used in the simulation of the double-plate impact experiments. This is a development from the previous replication studies and iterated to optimize the simulation settings. The chapter begins with an explanation of the simulation approach. The model geometry, material model and equation of state are then described, followed by a discussion of the boundary conditions. Then the details of the simulations are considered, such as contact setting and SPH particle parameters.

5.1. Simulation Approach

The behaviour of the debris cloud is highly unpredictable, therefore the explicit time integration is used in the simulation. This is a commonly used method for most crash and high-speed events. The explicit time integration uses the solution of a system of equations at each timestep to calculate the next one. This makes it appropriate for the simulation of highly non-linear, high-speed events. The timestep of the simulation has to be kept small to appropriately capture the details of the rapidly changing system. The appropriate value is automatically calculated, unless additional time step controls are employed, such as mass scaling, which is not used in this simulation.

As observed in the replication studies, SPH particles are used at the core of the simulation. This method has been chosen as it has been demonstrated to achieve high accuracy in modelling damage and the behaviour of the debris cloud.

A stepwise approach was used in the development of the simulation, starting with a single plate and progressively increasing the complexity. Single plate simulations were validated during the replication studies. In the next stage, the double plate system was created. Different simulation parameters were explored to increase the accuracy. To evaluate the effectiveness of different models, variations in the simulations were made and compared with the baseline. This approach allowed for the examination of the impact of different variables on the outcome. Once the most accurate model was determined, it was tested at various impact velocities, to create a model that accurately predicts the crater diameters of impacts at speeds ranging from 2.9 km/s to 7.2 km/s. The accuracy was measured by comparison of the crater diameter with the experimental value.

5.2. Simulated experiments

The thesis aims to develop and validate a simulation model using experimental data provided by the European Space Agency (ESA), courtesy of Airbus Defence and Space GmbH. These data were gathered at the Ernst Mach Institute and are presented in section 6.2. Experiments involved using a two-stage light gas gun to accelerate a 5mm diameter aluminium sphere into a double-layer Whipple shield.

The Whipple shield was placed in a fixed frame with support over the whole perimeter. An example of the Whipple shield set-up without the clamp at the perimeter is presented in Figure 5.1. The geometry of the impact zone is presented in Figure 5.2. There are two plates at a distance, representative of the sandwich structure with 60 mm spacing. In all experiments, both plates of the Whipple shield have been penetrated thoroughly. Therefore, the main goal of the simulation is to model and accurately

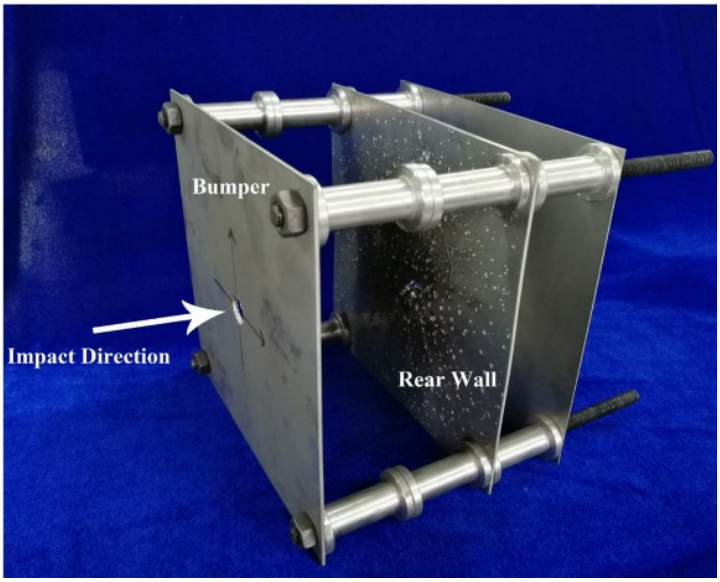

Figure 5.1: Picture of the example experimental set-up for hypervelocity impact [42]

predict the diameter of the damage zones. The diameter of the perforation is measured using the top view in the simulation. The influence of through-the-thickness changes is negligible, due to the small thickness of the plates. Perforation diameter is measured as described in Figure 5.2.

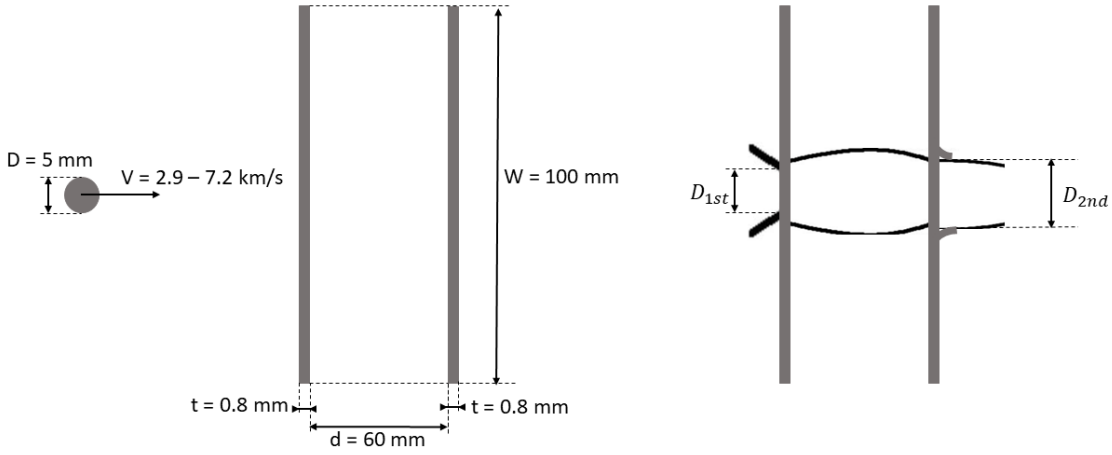

Figure 5.2: Representation of experiment setup (left) and measured output parameters (right) from the side view

5.3. Model Geometry

A big part of the simulation parameters is drawn from the replication work of Legaud et al. as described in section 4.1. Those parameters include mesh density, postprocessing and SPH control settings. Parameters of significant influence on the results such as material model or Equation of State were evaluated using the full double-plate system to determine the most suitable solution. However, some

parameters were only iterated using single-plate experiments. If a parameter has no theoretical reason to be of large influence and that was proven to be the case, it was used with the same setting as in the replication. On the other side, the mesh density was proven to be difficult to iterate due to the software limitations and extensive remodelling required. Nevertheless, mesh sensitivity was conducted to determine whether the mesh density used in the replication in section 4.1 was sufficient for the double plate model, as described in section 5.11.

The mesh parameters are tabulated in Table 5.1. The first plate in the simulation uses 691200 SPH particles arranged in a 250x250x12 matrix and has dimensions of 30x30mm, with a thickness of 0.8mm. The second plate has a larger SPH impact zone of 100x100mm, surrounded by a finite element outline with a side length of 230mm. The large FE surface area was used for the examination of the stress field around the area, as well as for connection to the boundary condition. The second impact zone is made up of 1225000 SPH particles arranged in a 350x350x10 matrix. The surrounding solid has 95424 elements, each with 3 elements through the thickness. The sphere consists of 33552 SPH particles. The goal of the meshing process was to provide a fine mesh with similar density across all three SPH parts, within the computational limits of the 32 CPU system and a target simulation time of fewer than 48 hours. Symmetry was not used in this simulation to avoid introducing additional variables that could influence the results.

	Dimensions of SPH zone [mm]	Number of SPH particles in principal directions	Total number of SPH particles in the part
1st Plate	30 x 30 x 0.8	250 x 250 x 12	691200
2nd Plate	100 x 100 x 0.8	350 x 350 x 10	1225000
Sphere	D = 5	40 x 40 x 40	33552

Table 5.1: Description of the mesh dimensions for the final double plate model

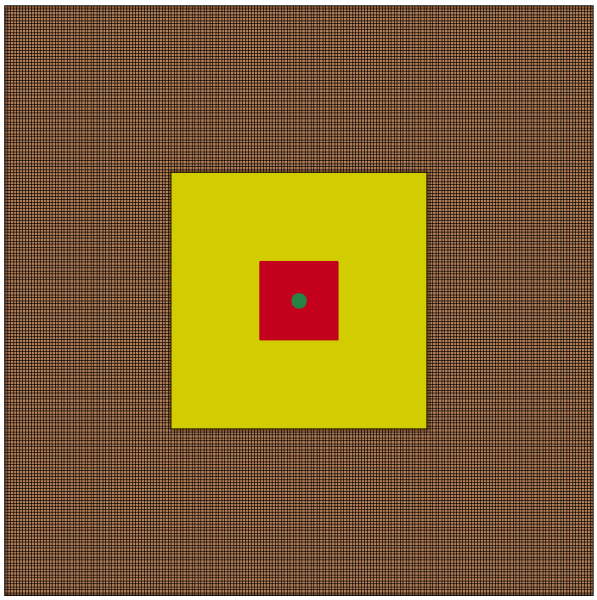

Figure 5.3: Comparison of sizes between the 2nd plate solid finite element zone (Orange), 2nd plate impact SPH zone (Yellow) with the first plate SPH zone (red) and the impacting sphere (green).

5.3.1. First bumper

The behaviour of the first bumper has been well-studied in literature, as this has been the first focus of the research. It is now well known, that the thin metallic bumper hit by a solid projectile gets perforated

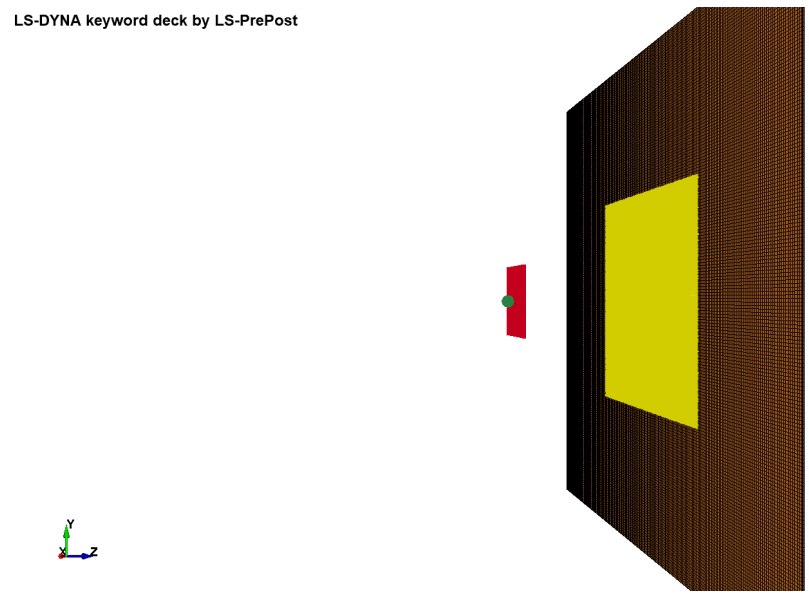

Figure 5.4: View of the mesh from the perspective. The distance between the first plate (red) and the second plate (yellow and brown) can be seen. The projectile (green) is very close to the plate, but it is not in contact at the beginning of the simulation.

forming a regular round hole in the aftermatch. A debris cloud is formed at the moment of impact, and the debris propagates further. The behaviour of the debris cloud is a much more complex phenomenon. It has been established in this research, that the size of the initial hole is less than 1.5 times the projectile diameter, leading to a relatively small damage zone.
When analyzing multiple plate tests, the debris cloud produced is a considerably greater and more significant feature. This is because the accuracy of the crater diameter in the first plate has been achieved reliably, but the simulation of the damage zone in the second plate hit by the debris cloud is ongoing research.

The accuracy of the debris cloud is dependent on the mesh density of the first plate. Therefore, the high-density mesh has to be employed in the zone of impact. Having a sufficient number of particles to form a realistic debris cloud representation is crucial. In reality, the size of particles in such debris clouds is very small. It is hard to distinguish individual particles as part of the material is melted and even vaporised. On the other hand, the debris cloud is produced from a relatively small portion of the plate directly interacting with the projectile. Therefore, the number of particles through the thickness of the plate is an important feature. It is also related to the accuracy of the hole diameter measurement [37]. This number determines how many 'layers' of SPH particles are created to form the plate, and it should be high for better accuracy. This drives the mesh density even further, as other dimensions of the plate are much larger than the thickness. The SPH particle performs best when the specific length in all three dimensions is similar, but this is hard to achieve while trying to maximize the number of particles through the thickness.
The first bumper is the reduced size of the plate with high-density packing. Therefore, a square of the size 30 by 30 mm is modelled instead of the full plate. This allows for high-density packing through the thickness and in both other directions, without a big burden on the computational performance. The edges of the crater are still sufficiently far away from the edges to not affect debris cloud formation. The minimum size of the plate is determined based on the speed of sound in the aluminium, which is 6.32km/s. The time span of the projectile being in contact with the first plate is around 2 µs, based on findings from replication studies, as seen in Figure 4.8. The distance travelled by the shockwave within the plate in this timeframe is 13mm in the radial direction from the centre. The plate of size 30mm will not interfere with the debris cloud formation, as the termination of the plate cannot interact the centre within the most crucial timeframe, due to speed of sound limitations.
The fixed boundary condition was not used at the edges for the first bumper, to not artificially stiffen the plate. The implementation of the boundary condition has minimal effect on the hole diameter. However, it is still recommended to avoid utilizing the fixed boundary condition for the sake of consistency and

theoretical completeness.

5.3.2. Second bumper

The second bumper is hit by a debris cloud consisting of fragments of the projectile and the first bumper. The cloud is significantly larger than the initial projectile and travels at a slightly reduced velocity to the initial impact - around 15% slower. To assess the damage done by such debris clouds, the model of the second bumper must be much larger than the first one. The zone affected by the debris is over 15 times larger than the initial projectile diameter, depending on the distance between the two bumpers. In the case of the impact at the normal angle, the cloud travels parallel to the initial velocity vector. Therefore, both the first and second bumper sustain damage in the form of concentric craters. This means that the high-density SPH zones can be located concentrically as well, simplifying the modelling. In the case of oblique impact, this would need to be adjusted as the debris cloud propagates in a different shape, necessitating an oblong SPH hit zone in the second bumper. However, in this work, only impacts at the normal angle are considered.
The 2nd plate has to be modelled with a bigger SPH zone. The minimum dimensions of the SPH zone depend on the size of the debris cloud at the moment of impact. This is a function of all impact parameters and crucially - the distance between two bumpers. Therefore, the single plate experiment was run first, and then the zone impact zone was approximated by the size of the debris cloud with sufficient spacing around the object. The second bumper has high-density SPH in the centre, surrounded by a larger FE zone. This is an efficient way of simulation of larger objects that require fine detail in one location.
The SPH zone shall be big enough that the main debris cloud can impact it with a sufficient margin around it. As it is shown in the section 6.1 the debris eventually spreads to encompass a large area of the simulation. However, the initial, destructive jet of debris is investigated. This cloud has a clear definition and has to be contained within the SPH zone.
The plate is surrounded by the zone of Finite elements, which do not have defined contact with SPH particles. Finite elements are used to provide a buffer zone from the fixed boundary condition to the high-density SPH zone. It is more computationally efficient than enlarging the SPH zone.

5.3.3. Projectile

The projectile is a sphere with a 5mm diameter that has been modelled using SPH. The sphere undergoes near-total disintegration during impact with the primary bumper. Therefore, it is modelled using SPH particles just as the central zones of the plates. The sphere is formed using the default option in LS-DYNA that allows for the creation of basic geometric shapes. To create such an object, it is necessary to input the number of particles in three principal directions. This determines the packing density of particles within the sphere. The packing density shall be close to the one used in the plates. This enables correct collision registration and debris cloud propagation. To match this criterion, the 40x40x40 matrix has been employed.
The projectile is located at the centre of the hitting zone in front of the 1st plate. It is placed very close to the plate to minimize the time of simulation where it travels through empty space. However, the objects are not touching at the initiation of the simulation. The sphere is given the initial velocity using the INITIAL_VELOCITY_GENERATION keyword card, as it provides the initial velocity to the part, as opposed to the sustained velocity that INITIAL_VELOCITY generates. The velocity is determined based on the experiment specification.

5.4. Material model

The material model plays a crucial role in the behaviour of the component upon impact. The appropriate choice of model is necessary for the simulation to be accurate. Therefore, the lessons learned from the previous 2 replications were applied to find the most appropriate model. Moreover, different models were explored with the use of a double plate system to determine which one of the available candidates produce the most accurate results.
The Johnson-Cook model was adopted in this study because previous simulations demonstrated that it is the most appropriate. The Johnson-Cook model is supported by its common use in literature [33] and has proven to model the crater diameter accurately in the replication study, as given in Table 4.8. Johnson-Cook plasticity describes materials under large strain, high strain rates and high temperatures.

The key concepts in such events are:

- Strain hardening
- Strain-rate effects
- Thermal softening

The model combines all three into a single equation. Strain hardening is a phenomenon when ductile metal becomes stronger and harder as a result of plastic deformation. For pure metals, it can be explained as a result of increased dislocation density. Dislocations are misalignments of the crystalline lattice of the material.

The plastic deformation of metals is essentially a movement and creation of large numbers of dislocations. As the motion of the dislocation is hindered by other dislocations, the material exhibits greater resistance to deformation. Strain-hardened material has therefore higher yield stress, at the cost of reduced ductility.

Strain rate effects are relevant for events happening at high speed. During rapid straining of the material, it changes its stiffness. This effect has an especially significant effect when the speed of sound in the material is exceeded by the projectile.
Lastly, thermal softening relates the temperature of the material to its properties. The material model is based on the following equation

$$\sigma_y = \left(A + B\bar{\varepsilon}^{\mathrm{p}^n}\right)\left(1 + c\ln\dot{\varepsilon}^*\right)\left(1 - T^{*m}\right) \tag{5.1}$$

with following definitions

$$T^* = \frac{T - T_{\mathrm{room}}}{T_{\mathrm{melt}} - T_{\mathrm{room}}} \tag{5.2}$$

$\bar{\varepsilon}^p$ where σ_y is the yield stress, $\bar{\varepsilon}^p$ is the effective plastic strain, A, B, N, c, m are material constants T is the temperature, T_{room} is the reference room temperature and T_{melt} is the melting temperature of the mateiral. The first term A is the initial yield stress, and the second term $B(\bar{\varepsilon}^p)^N$ is the work hardening term, which describes how the strength of the material increases with increasing plastic strain. The third term represents the thermal softening and damage accumulation of the material.

Both bumpers are made of Al 2024-T3, which is commonly used in various structural applications and for which there is a significant amount of literature available using the Johnson-Cook model. The projectile was made from Al 2007, which does not have easily available Johnson-cook parameters. Both Al 2024-T3 and Al 2007 are high-strength, heat-treatable alloys but have differences. Aluminium 2024 is an Aluminium-Copper-Iron alloy with a yield strength of around 275MPa. It is commonly used in aerospace due to its high strength-to-weight ratio, relatively good stiffness and good surface finish. The Al 2024-T3 heat treatment involves heating the alloy to high temperatures and rapidly cooling it, creating precipitation and hardening second-phase particles. Such alloy is then cold-worked which further increases its hardness. At last, it is naturally aged.
Al 2007 is an Aluminium-Copper-Magnesium alloy with a lower yield strength of around 240MPa. The heat treatment was undisclosed in the experimental data. It is also a precipitation-hardened alloy, used for high-strength applications that require good corrosion resistance. There is considerably less research on the modelling of this material when compared to Al 2024. No complete Johnson-Cook model was found in the literature for this alloy, therefore replacement measures were taken.
According to the research from Nestor and Clough [43], the driving parameter in the penetration capability of the projectile is its density. At high speeds, the material strength properties cease to affect the results. This is because the pressures involved in the impact are well beyond the strength of the material [44]. Guo et al. confirmed this trend for impacts as slow as 0.3 km/s [45]. As both alloys have comparable density and properties in general, the Johnson-Cook model for Al 2024-T3 is used for a projectile, as a replacement for the Al 2007 model. A slightly higher yield strength of the Al 2024-T3 will have minimal effects on the results, as it is not the driving parameter in the penetration.

The parameters in the Johnson-Cook material model have been experimentally found in different publications. Two best candidates were found in the study from Lacome et al. [39]and FAA. [46]. Those documents provided a complete description of parameters at similar conditions as observed during impact. Two models are used for the same material but with different parameter settings. To determine the best one, both were tested in the double-plate system. The governing factor for each was how close the diameter of the damage zone is to the original value. The results of this experimentation are presented in section 6.5.

	Al 2024-T3	Al 2024-T3
Publication	Lacome et al. [39]	FAA[46]
Density [g/cm3]	2.785	2.785
Shear modulus [Mbar]	0.286	0.286
A [Mbar]	0.00265	0.00369
B [Mbar]	0.00426	0.00684
c [-]	0.015	0.0083
n [-]	0.34	0.74
m [-]	1	1.7
Specific heat $[10^7 \frac{Ncm}{gK}]$	0.875e-5	0.875e-5
Melt température [K]	775	775
Room temperature [K]	273	294

Table 5.2: Johnson-Cook Material model parameters

5.5. Failure Criteria

The additional inputs in the LS-DYNA Johnson-Cook material model are fracture parameters. Those parameters are optional and the values are used to determine the strain at fracture, represented by following equation:

$$\varepsilon^{\mathsf{f}} = [D_1 + D_2 \exp{(D_3 \sigma^*)}] [1 + D_4 \ln{\varepsilon^*}] [1 + D_5 T^*] \tag{5.3}$$

where D1 is the material constant that describes the relationship between the plastic strain rate and the equivalent plastic strain, also known as the hardening parameter. D2 describes the relationship between the plastic strain and the material's strength. D3 is the constant that describes the thermal softening effect which increases the strength of the material at high temperatures. D4 controls the rate at which the material's strength increases with increasing strain. D5 determines the rate of thermal softening with increasing temperature [47].
Experimentation with those parameters was performed to determine their effect on the result. In the hypervelocity simulation literature, the usage of this additional failure condition is omitted [37] [39]. To find their influence on the result, the complete material models were found with the failure criteria included.

To investigate the influence of those criteria, additional simulation was performed. The simulation used inputs included in this chapter, with the Johnson-Cook material model, as given in Table 5.2. The double-plate mesh pictured in Figure 5.3 was used. A comparison was done between the original model which did not take into account any fracture criteria and the new model which included the criteria, shown in Table 5.3. The complete material model can be found in the publication from Federal Aviation Administration (FAA) [46]. The results of this experimentation are presented in subsection 6.5.1.

	Al 2024-T3
Publication	FAA [46]
D1 [-]	0.31
D2 [-]	0.0045
D3 [-]	-1.7
D4 [-]	0.005
D5 [-]	0

Table 5.3: Fracture criteria used in the simulations to determine their impact on the result

5.6. Equation of State

The equation of state (EOS) is a mathematical equation that describes the relationship between the state variables, such as pressure, volume, and temperature. The use of the SPH technique requires the use of EOS to define the behaviour of the particles. During the hypervelocity impact, very high pressures and temperatures are present. This necessitates the use of EOS that is appropriate to such conditions. The most commonly used EOS for solids under hypervelocity impact is the Gruneisen equation [3] [33]. At first, the values from Legaud et al. for Al 6061-T6 were used as they were tested in the replication study. In the official simulation, however, the values were modified to better match the Al 2024 profile, using values from another work by FAA [46]. The Mie-Gruneisen equation of state is a mathematical model that is particularly suited for use in high temperatures and pressures present in the hypervelocity impact.

The model uses cubic shock velocity as a function of the particle velocity in LS-DYNA for compressed materials is defined by the following equation:

$$p = \frac{\rho_0 C^2 \mu \left[1 + \left(1 - \frac{\gamma_0}{2}\right)\mu - \frac{a}{2}\mu^2\right]}{\left[1 - (S_1 - 1)\,\mu - S_2 \frac{\mu^2}{\mu+1} - S_3 \frac{\mu^3}{(\mu+1)^2}\right]^2} + (\gamma_0 + a\mu)\,E \tag{5.4}$$

and following for expanded materials:

$$p = \rho_0 C^2 \mu + (\gamma_0 + a\mu)\,E \tag{5.5}$$

with

$$\mu = \frac{\rho}{\rho_0} - 1 \tag{5.6}$$

and C is the intercept of the $v_s\,(v_p)$ curve, S_1, S_2, S_3 are unitless coefficients of the $v_s\,(v_p)$ curve. γ_0 is the Gruneisen gamma - unitless. First-order correction to the γ_0 is present in the equation as a/ and E represents the internal energy. The μ is dependent on the ratio of the current density ρ to the initial density ρ_0.

	Al 6061-T6	Al 2024 -T3
Publication	Legaud et al. [37]	FAA [46]
C	0.524	0.524
S1	1.4	1.338
S2	0	0
S3	0	0
Gruneisen parameter γ	1.97	2
A parameter	0.48	0.48
Initial Internal Energy	0	0
Initial Relative Volume	0	0

Table 5.4: Gruneisten Parameters Comparison

5.7. Contact

The contact settings can be divided into two main areas. The first one is governing the impact behaviour between different SPH parts, and the second is used to join SPH particles with Finite Elements.

5.7.1. SPH to SPH contact

The choice of contact formulation is important in governing the impact dynamics between the projectile and the second bumper, as well as the behaviour of the debris cloud itself. Two main types of contact can be used between SPH parts: the particle approximation and the penalty method. The penalty method is often used with finite elements because of its efficiency, stability, and reliability, but it is not well-suited for modelling hypervelocity impacts. When objects undergo fundamental changes during impact, behaving more like a fluid, the penalty method is unable to accurately compute all interactions between particles. As a result, objects may pass through each other with minimal distortion when this method is used. There are variations of the penalty method, such as the Soft Constraint Penalty Formulation and Segment-based Penalty Formulation, which can improve its accuracy in certain situations, such as when modelling contact between objects with dissimilar stiffness or airbag simulations. However, these variations do not address the fundamental limitations of the penalty method in modelling hypervelocity impacts.

The alternative to the penalty method is the particle approximation method, which is a feature of SPH. This method treats different SPH bodies using the same physical laws that govern their intrinsic behaviour. This is an effective way to model contact, both for the initial impact and for the propagation of debris. The particle approximation method can replicate the mixing of projectile and bumper material during impact, which results in a coherent debris cloud. This method is defined by setting the card CONTROL_SPH_CONT to 0 - a different CONTACT card is not required for this setting to function.
The particle approximation method in SPH treats all related parts as particles and ensures consistent interaction between them. This method is superior to other contact formulations, such as the penalty method, which defines interaction on a part-to-part basis. The particle approximation method allows for more accurate modelling of the initial hit and the propagation of debris during hypervelocity impact.

5.7.2. SPH to FEM contact

Two ways have been employed to bond the particles to the solid elements around them. The difference is in the use of the transition zone made of hybrid SPH/FEM elements. The use of this zone smoothens the transition and enables more accurate propagation of stress to the elements outside. This zone uses elements formed by the DEFINE_ADAPTIVE_SOLID_TO_SPH keyword. To create a such zone, the ICPL setting is set to 1 and the IOPT setting is equal to 0 within the keyword. The former determines whether the SPH is coupled to the solid element or is free to move. To provide a smooth transition, the SPH within the hybrid element has to be coupled to the solid. The latter setting ensures that this coupling is active immediately from the start of the simulation. The CONTACT_TIED_NODES_TO_SURFACE keyword is used to bond two pieces together. This is the preferred method of joining those two types of entities.

5.8. SPH parameters

The control settings of the SPH particles have an important role in ensuring the stability and accuracy of the simulation. Those settings determine the interactions between particles.

A CONTROL_SPH card was used to control the properties of the SPH particles. One such property is a deactivation box, which was used to deactivate SPH particles outside of its boundaries to improve computational efficiency. The box was designed to encompass all the features in the structure, including the secondary debris cloud and ejecta veil, with a margin. In the related setting, SPH is configured to be three-dimensional.
The number of neighbours of the particle significantly increased from 150 to 850. The change is necessary to be able to process the complicated interaction of debris with the second plate. The automatic process of determination of neighbours leads to a crash of simulation if the initial number is not high enough. Following the neighbour number, the default SPH formulation has been chosen. Legaud et al. performed a study comparing the SPH formulation with the accuracy of crater diameter measurement and concluded that the default formulation is the best choice for hypervelocity impacts [37]. Moreover,

tests conducted with fluid formulation have confirmed that the default leads to more consistent results. The following feature in the CONTROL_SPH card is the definition of interaction between two different SPH parts. The particle approximation was defined - this means that two different parts interact using the same mechanics as the parts internally. This enables both accurate hit recognition as well as debris cloud dynamics. This is in opposition to the commonly used penalty method, which was unable to correctly track and compute the contact between many small debris pieces and the bumper. Artificial viscosity is used to propagate discontinuities across multiple particles and to prevent tensile instability. Two types of viscosity are available in LS-Dyna. Monaghan type which was described in the literature by the authors of the SPH approximation [48] and solid element viscosity. The behaviour at the impact zone cannot be described as a simple solid structure, and Monaghan viscosity is more universal. Therefore it has been used in the simulation. Finally, incremental stabilisation was chosen as the total stabilisation shall only be used in hyperelastic materials.
Further settings regarding SPH particles were added in SECTION_SPH card. This card is mainly used to determine constant multiplying the smoothing length of the particles. Available settings are the initial constant and then the minimum and maximum allowable constant during the simulation. In the final version of the simulation, the recommended initial value is used of 1.2, with a minimum and maximum of 0.2 to 1.5.

The simulation time controlled by the card CONTROL_TERMINATION has been varied depending on the objective of the simulation. In the first 50 μs the impact into the second bumper occurs, but more time is necessary for the impact to fully develop and for debris to be removed from the site. Therefore, the simulation up to 400 μs was conducted, with the first 100 μs considered to be the most vital. No additional termination criteria were used.

5.9. Finite Element properties

The area that surrounds the SPH in the second plate is made from finite elements. As their nature is different, therefore it requires changes to modelling cards to function correctly. This is predetermined in the software. The main feature that needs to be modified is SECTION and HOURGLASS keywords. The section keyword is specific for every kind of modelling technique. In this case, SECTION_SOLID is used for finite elements. Despite the thin nature of the bumper plate, the shell elements were not used, as the interaction between the shell elements and SPH would be problematic. The main variable to be chosen in the section card is the element formulation. Constant stress solid element was chosen. This element type is accurate, efficient and works well even under severe deformations. However, it requires hourglass stabilization. Therefore HOURGLASS card is used, with the Flanagan-Belytschko viscous form type. This type is appropriate for high-velocity cases. It is recommended type by the LS-Dyna manual and has been used for hypervelocity simulation in the literature [41]. The main benefit of this type of viscosity it has a negligible effect on the energy in the system.

5.10. Massively Parallel Processing

LS-DYNA offers two main versions of the program. The basic version is Symmetric Multi-Processing (SMP). It is designed to be operated on a limited number of processors and originated from the serial code. The workload is split between processors using the same data bus. The peak efficiency per processor declines at CPU numbers higher than 8. Consistency among the processors is ensured at the cost of efficiency.
Massively Parallel Processing (MPP) is an alternative version of LS-Dyna that uses the spatial domain decomposition method. It distributes the sub-domains of the problem to different cores. It uses the message-passing protocol to transfer information between different cores. This enables efficient operation at a very high CPU count. Moreover, the processors are not required to be connected to the same cluster node during the operation but can exchange information directly. The disadvantage of this system is the results of simulations using different decomposition techniques and the number of cores might differ. The problems with consistency and possible influence on the result have to be accounted for when using the MPP. The benefits of this version are the biggest when dealing with large simulations and using over 32 processors.
The methods have been compared directly when the replication of Plassard et al. has been performed. It was determined that the SMP method provides more consistent results and describes the stress field

in the SPH in a more realistic manner. The difference is especially visible when examining the stress field in the SPH region.
The logic behind the MPP processing is that different parts of the model can be computed independently. However, the detailed simulation of impact into the Whipple shield is progressive and heavily depends on the initial contact and subsequent debris cloud. The MPP is much more suitable for the simulation of large objects. Additionally, 32 processors are sufficient for processing the current simulation within a relatively short timeframe of several hours.

5.11. Mesh Convergance Study

	SPH Part	Number of SPH in principal directions	Number of SPH	Total SPH count
1	1st Plate	100 x 100 x 10	1000	230224
	2nd Plate	150 x 150 x 10	225000	
	Sphere	20 x 20 x 20	4224	
2	1st Plate	90 x 90 x 9	72900	907364
	2nd Plate	300 x 300 x 9	810000	
	Sphere	36 x 36 x36	24464	
3	1st Plate	100 x 100 x 10	691200	1949752
	2nd Plate	350 x 350 x 10	1225000	
	Sphere	40 x 40 x 40	33552	

Table 5.5: Description of the three different simulations used for mesh convergence study

The mesh convergence study is an important step in numerical simulations. The damage from hypervelocity impact occurs at very small length scales, requiring high-resolution mesh to capture the details of the behaviour. The solution of the simulation should be mesh-independent, meaning that the solution does not change with further mesh refinement.
The SPH is a meshless method, the convergence is conducted by varying the number of SPH particles in the part. The bigger the number of particles, the finer the resolution of the simulation. Therefore, the convergence study requires running the simulation multiple times with different numbers of particles and comparing the result. The simulation is deemed to be convergent if the difference in the result between two mesh densities is within a specified tolerance. This is often described as an asymptote in the error graph. In this study, the cut-off value of 5% is used. The parameter examined in the convergence is the crater diameter of the 2nd plate. This is because the value is the primary focus of this research.
The study is conducted at the impact velocity of 5.4 km/s, using the Johnson-cook model and Gruneisen EOS sourced from FAA[46]. All parameters are kept identical with the exception of the SPH grid. That is to ensure that the study is representative of the model used to obtain other simulations. The convergence study is conducted using three models. The description of the mesh is given in Table 5.5. Model number 1 has the lowest number of SPH particles, equating to 12% of the finest model. It is therefore much less computationally demanding. Created with around half of the particles in principal directions, with exception of thickness. The thickness, due to a much smaller initial number of particles, was kept constant. The second model was aimed to have SPH count around 50% of the final model. This was achieved by reducing the number of particles in all principal directions by around 10%. The 3rd model represents the full fidelity simulation that is used to obtain results regarding the crater diameters.
The low fidelity simulation number one has proved to be ineffective in replicating the desired behaviour. The formed craters were of very different dimensions compared to fine simulations and experiments. This is expected, as the lack of error after such a big reduction of SPH count would indicate that the full-fidelity simulation uses much more particles than required and is computationally inefficient.
Simulation number two, which uses 53% fewer particles, has proven to capture the majority of the behaviour at a lesser computational cost. The simulation achieved results which are within 3 % of the full fidelity simulation. This matches the cut-off value in the study and enables the description of the asymptotic behaviour of the residual curve. As seen in Figure 5.5, using three data points and drawing a line at a 5% cut-off value, a convergence with respect to the full fidelity simulation has been obtained. The Figure 5.6 displays the behaviour of simulation number two.

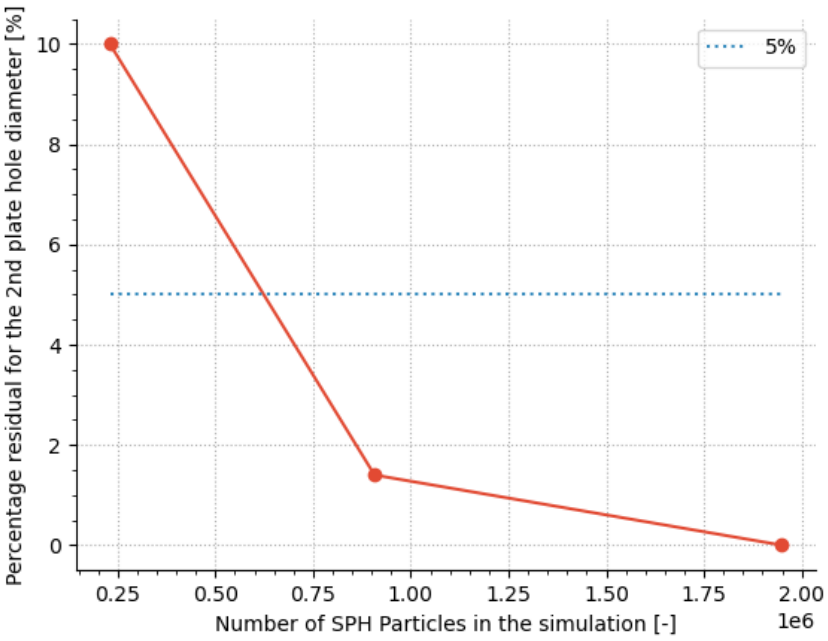

Figure 5.5: Mesh sensitivity plot of percentage residual with respect to the finest mesh. The mesh can be deemed convergent as the residual for the mesh with 50% of nodes is within the 5% cut-off value.

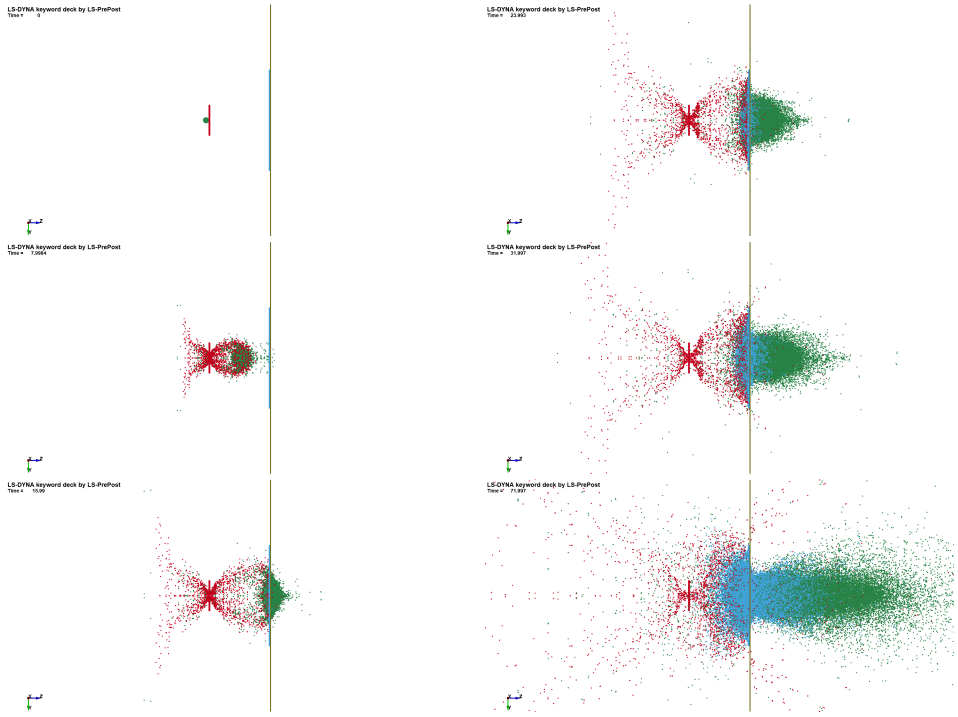

Figure 5.6: Propagation of the debris cloud in the simulation number two used for mesh sensitivity study in the first 70 µs after impact for impact at 5.4km/s

6

Results

This chapter presents the findings of the study, including the data and analysis obtained from the experiments and numerical simulations. It aims to provide an overview of the results and the conclusions that can be drawn from them.
Firstly, the general behaviour of the system is presented, followed by experimental data. Next, the results of the series of simulations are compared to those experimental values. The variations of simulations and the influence of changes in parameters are highlighted afterwards. Finally, an analysis of the results and important findings are described.

6.1. General behaviour

The formation of the debris cloud is a complex phenomenon that depends on a variety of factors. However, the majority of the qualitative features remain constant for a wide span of the input parameters and can be therefore characterised as such. The same features have been observed in the literature [6].

At the initial contact of the 1st plate with the sphere, the ejecta veil is formed. This can be observed in on the left side of Figure 6.1, which pictures the evolution of debris cloud for the impact at 2.9 km/s. The same timeframe for an impact velocity of 5.4 km/s is shown in Figure 6.2. The behaviour of the cloud at 7.1 km/s is pictured in Figure 6.3. The main difference between different velocities is the speed and the size of the debris cloud.
The debris ejected to the outside of the structure consists mostly of the material from the plate, rather than the projectile. Ejected particles are a long-term threat as they increase the total amount of debris in orbit. However, they are beneficial for dissipating the impact energy and reducing the penetration potential of the projectile. The damage is highly unlikely to be contained in the first plate, even if armour of excessive thickness is used. Therefore, the primary debris bubble forms behind the first plate. This bubble consists of a combination of projectile and plate material. It can be noticed that the projectile material is at the centre of the debris bubble, surrounded by the plate material from all sides. The cut-away view of the debris cloud is presented in Figure 6.4. The debris from the sphere is surrounded by the material from the first plate of the Whipple shield.
The properties of this central zone determine the destructive capability of the cloud. If the impact caused the complete disintegration of the projectile and fine debris is created, then the ability to penetrate the second plate is reduced. On the other hand, the presence of large fragments is tied to a greater risk of penetration.
Only the contact between SPH particles is modelled. Therefore, any particle that might head towards the FE part of the plate passes through without interaction. This is acceptable behaviour, as those particles are beyond the main damage zone and have no influence on the crater size.

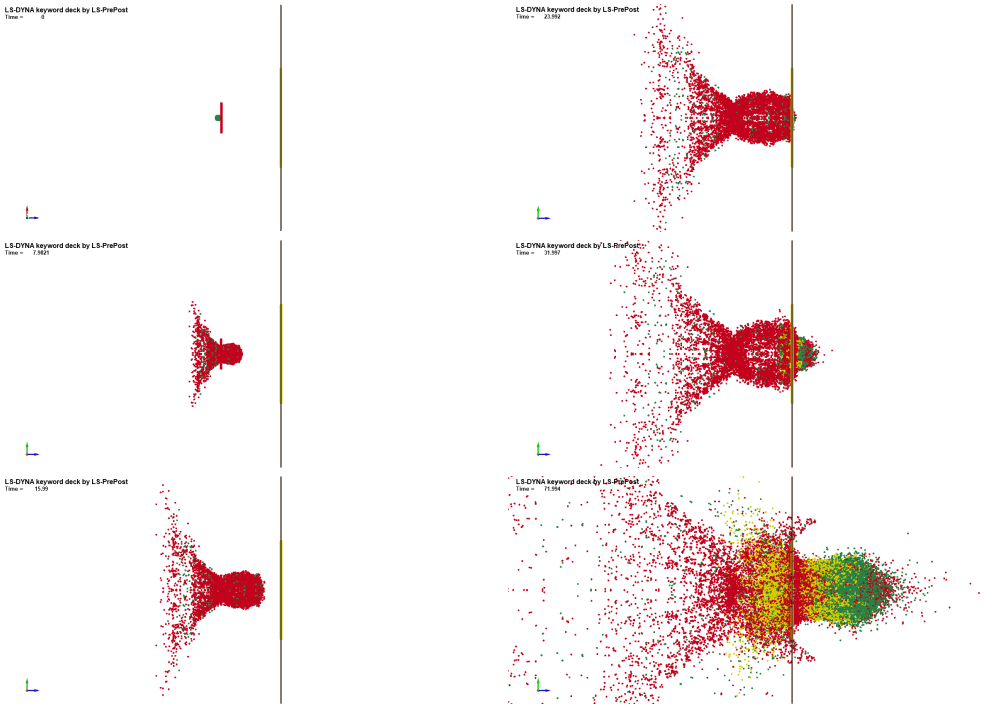

Figure 6.1: Propagation of the debris cloud in a double-plate experiment in the first 70 µs after impact for impact at 2.9km/s

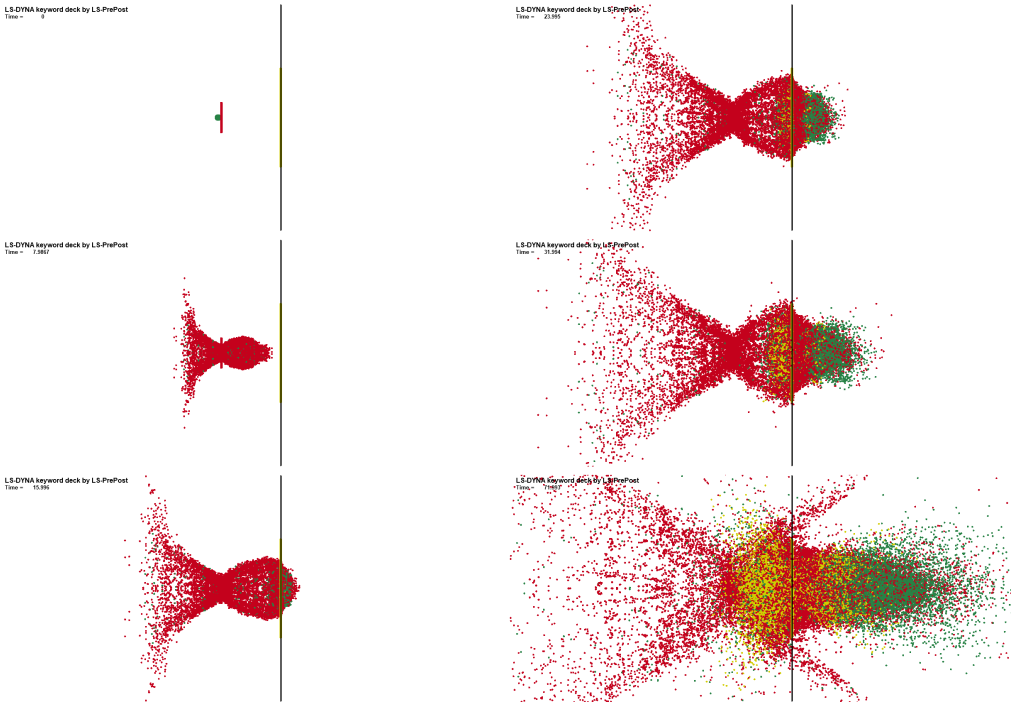

Figure 6.2: Propagation of the debris cloud in a double-plate experiment in the first 70 µs after impact for impact at 5.4km/s

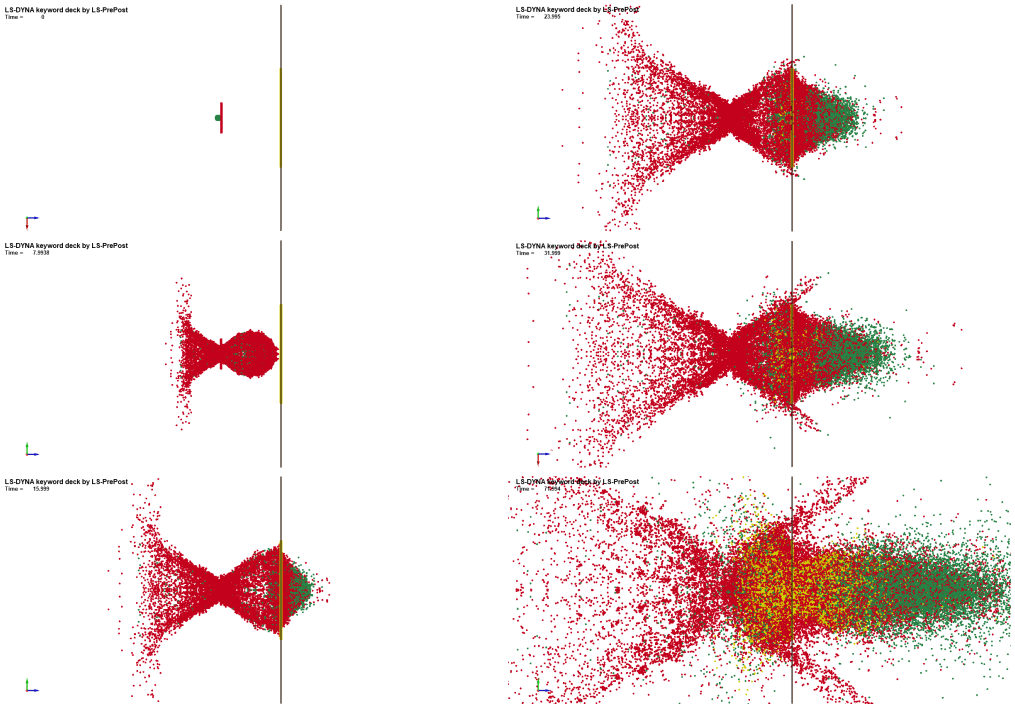

Figure 6.3: Propagation of the debris cloud in a double-plate experiment in the first 70 µs after impact for impact at 7.1km/s

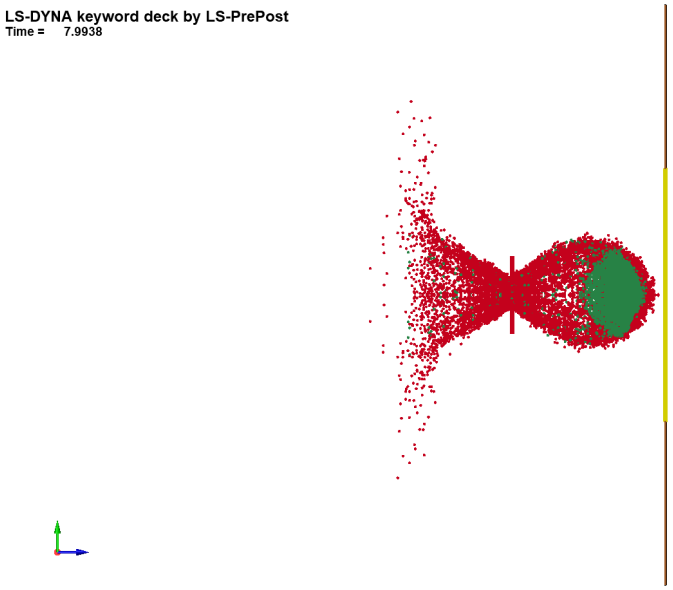

Figure 6.4: View inside of the debris cloud within the first 8 µs after impact at 7.1km/s. The material from the projectile is surrounded by the remains of the first plate.

6.2. Experimental data available

The data set used for the validation of the simulation is sourced from Airbus Defence and Space GmbH. This data has been collected during experiments performed at the hypervelocity facility at the Ernst Mach Institute. The experiment consists of a double plate Whipple shield impacted by the projectile at speeds from 2.9 to 7.2 km/s and is presented in Table 6.1. The comparison of this data is shown in Figure 6.5. The plates are made out of Al 2024-T3 and the projectile is from Al 2007. The dimensions of both impacted plates are 10mm by 10mm with a thickness of 0.8mm and spacing between the plates of 60mm. The projectiles are spheres of diameters either 5mm or 6mm. 10 experiments were conducted

and therefore the sample size is limited.
The examination of the numbers indicates that the results are not entirely repetitive, as the crater in 2nd wall can vary greatly between two shots of similar velocity. Experiment 4.1 requires special attention, as the diameter of the second hole is much smaller than in other experiments, despite the bigger velocity when compared to the experiment. This is an important consideration when the simulation is compared. On the other side, the crater size in the primary bumper is consistently increasing with greater impact velocity, with a small spread of results.

Test	Impact Velocity [km/s]	1st bumper Hole Diameter [mm]	2nd bumper Hole Diameter [mm]	Velocity behind the 2nd bumper [km/s]
25	7.1	9.3	58	-
25a	7.2	9	40	-
24	5.4	7.8	25	-
24a	5.4	7.9	24	-
4.1	3.1	7	11	-
4.2	2.9	6.7	27	1.2

Table 6.1: Experimental data used for validation of the simulation.

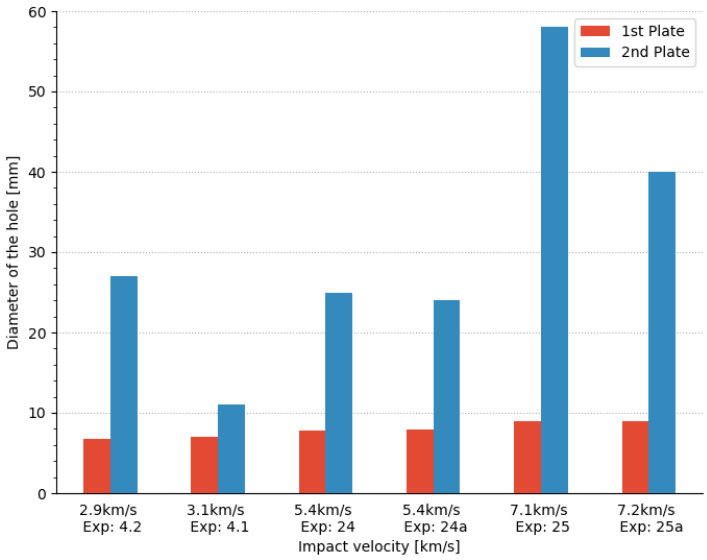

Figure 6.5: Plot displaying the results of the experiments. The damage was presented in ascending order of impact velocities. Courtesy of Airbus Defence and Space GmbH.

6.3. Velocity Profile

The velocity profile is examined as it indicates the penetration potential of the debris cloud. The velocity of the debris after each plate is one of the crucial factors determining further damage possible by the fragments. The fastest debris resides in the front of the cloud. The velocity of fragments has to be correlated with the mass distribution across the cloud. A cloud with high mass at the peak velocity has more destructive capacity compared to one where the majority of the mass is trailing behind at a low speed.
The velocity profile of the cloud behind the 1st bumper is characterised by a majority of mass at the peak of the cloud travelling at speeds higher than 80% of the impact velocity. This has been computed by counting the number of elements at the high and low-velocity zone. As the density and volume of each particle are kept constant, the count of particles enables the determination of the mass at a given

velocity. The particles at the peak of the debris cloud have higher velocity than the ones trailing behind, as observed on Figure 6.6. This quantitative method enables insight into the mass distribution that determines the destructive power of the debris cloud.
At a velocity impact of 2.9 km/s Over 80% elements are forming the peak of the primary debris cloud at velocities above 90% of the impact velocity. This means that the majority of mass in the cloud retains the high velocity of the impact. In contrast, the secondary cloud has very different behaviour. Less than 2% of the secondary debris cloud retains the velocity above 90% of the initial impact. The majority of the mass of the secondary debris cloud moves at less than 20% of the initial velocity. This is an important finding, as the damage potential of the secondary cloud is much smaller, despite the clouds having the same peak velocity when singular particles are considered.
In the experimental data, there is only one reading of the velocity after 2nd bumper. It for impact velocity of 2.9 km/s. The velocity of the debris cloud after 2nd plate was indicated to be 1.2 km/s. This can be correlated with the simulation. The peak velocity of the secondary debris cloud of experiment 4.2 is 3km/s. However, only singular particles have retained this speed. On the other side, 99% of the cloud mass has a velocity equal to or lower than 1.3km/s. The velocity profile for this case is pictured in Figure 6.6 and the plot indicating the comparison between simulation and experiment is given in Figure 6.9.

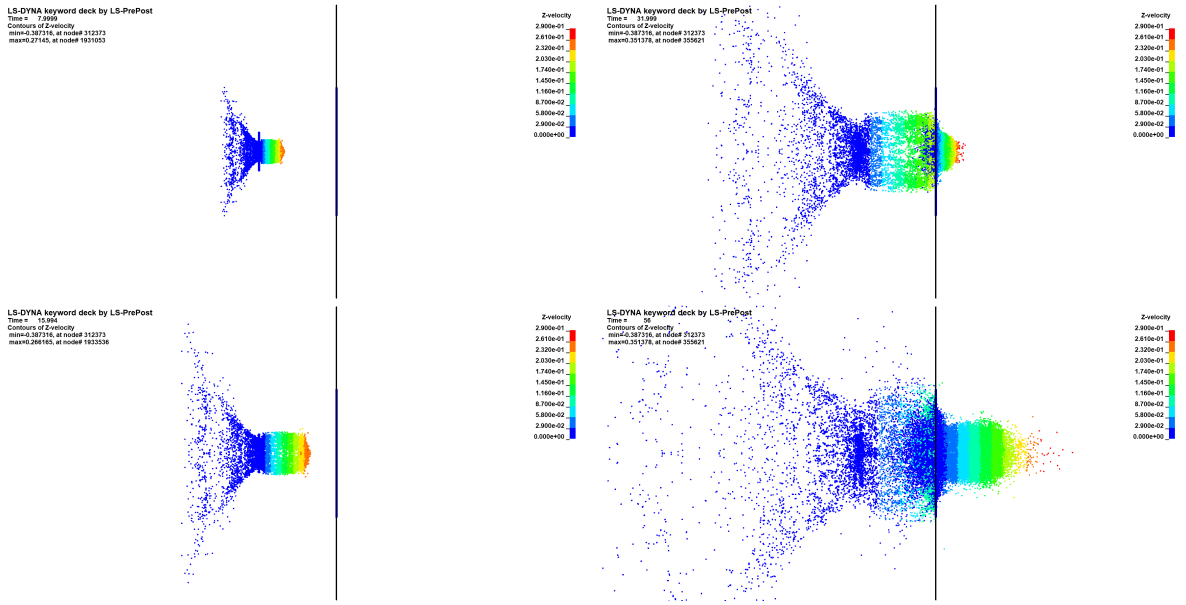

Figure 6.6: Velocity profile at an impact velocity of 2.9 km/s

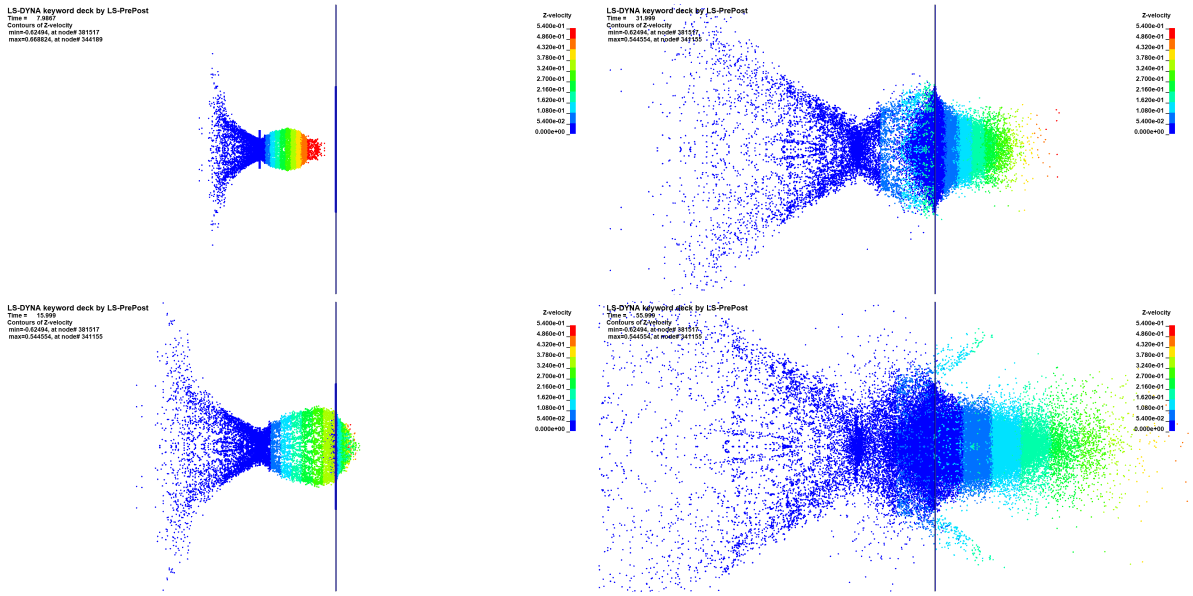

Figure 6.7: Velocity profile at an impact velocity of 5.4 km/s

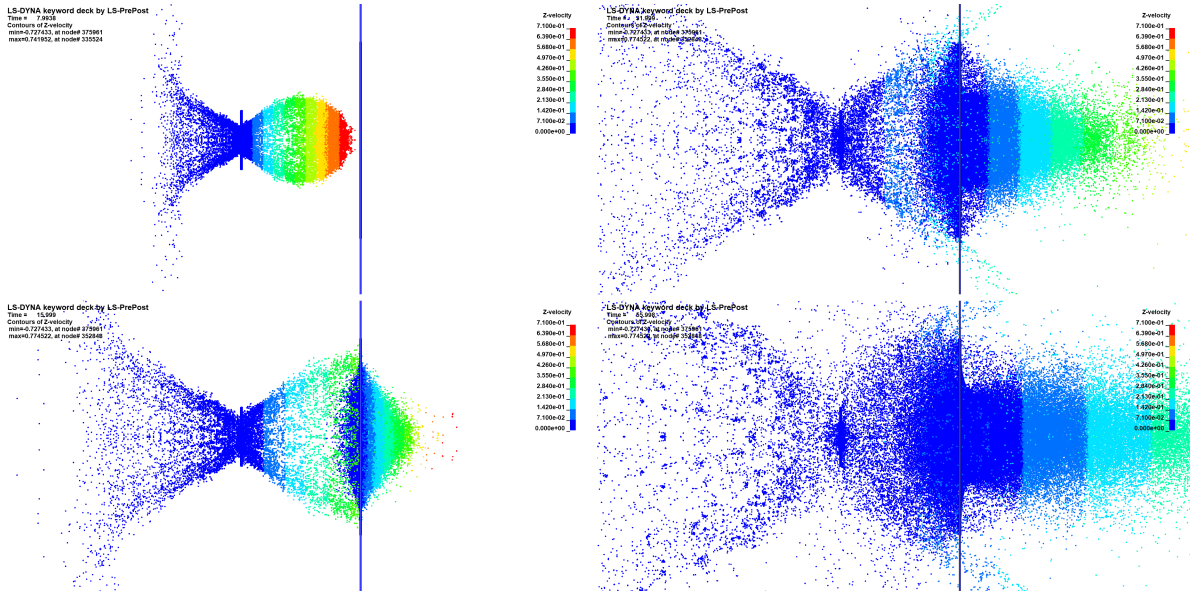

Figure 6.8: Velocity profile at an impact velocity of 7.1 km/s

If the impact is not contained by the 2nd plate, the debris continues travelling through the cavity at significantly reduced velocity. As a result, the destructive power of a such cloud is much smaller. Over 80% of primary debris cloud mass after 1st plate retains around 90% of the impact velocity. The large amount of mass that retains the velocity is dispersed and in much smaller fragments, but the velocity is kept high.
On the other hand, the secondary plate captures the debris at a much greater area, considerably slowing the debris cloud. This is an example of the high effectiveness of the Whipple shield at sustaining impacts. Even though it is penetrated, the secondary debris cloud has much lower damage potential. This behaviour is pictured for an impact velocity of 5.4km/s in Figure 6.7. The velocity profile for impact at 7.1 km/s is shown in Figure 6.8. In both figures, the velocity loss is greatest after impact with the 2nd wall.

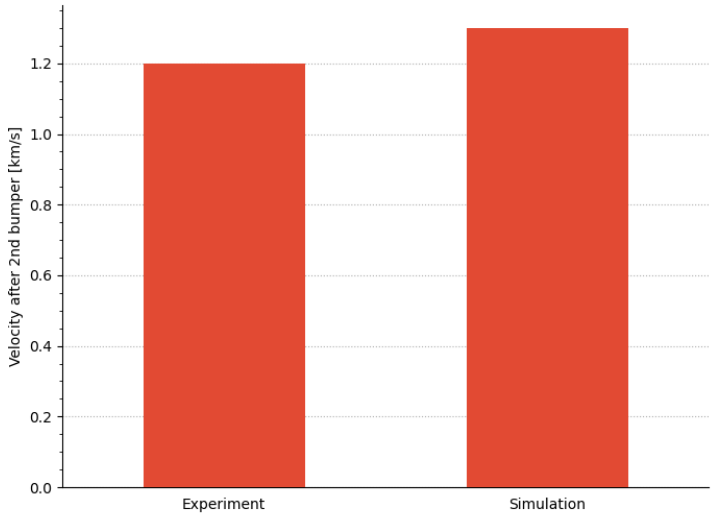

Figure 6.9: The comparison of experimental data from velocity measurement with the simulation. The velocity was measured behind the 2nd plate. Experimental data acquired courtesy of Airbus Defence and Space GmbH.

6.4. Results at different velocities

The main focus of the thesis is an investigation of the damage to the Whipple shield. The parameters measured in the experiments available are the diameters of the crater. Therefore the simulation of the crater size is of the primary concern. The focus is on the simulation and validation using experiments performed using the 5mm projectile at a speed from 2.9km/s to 7.1 km/s. This section presents the results at each respective velocity.

6.4.1. Impact velocity = 7.1 km/s

This is the highest of the velocities examined in the study. Close correlations have been observed with the experiments. The shape of the hole in the first plate is nearly perfectly circular, pictured in the middle of Figure 6.11. In the figure, both plates can be seen, from the top view. The smaller first plate model is visible throughout the perforation in the second plate. The damage zone in the second crater is much less regular, with the diameter measurement being correlated with the experiment within 30%, large cracks are formed in four directions from the impact zone, making the diameter measurement difficult. As with all other velocities, the damage in the initial zone is very close to the one measured in the experiment.

The measurement is performed at the transition between the circular damage zone and the crack formation. This gives a middle ground between the smallest possible diameter and a much larger span from crack tip to crack tip. This is consistent with other measurements in the study. The result is within 10% to 30% of the experimental value.
The data is tabulated in the Table 6.2 and represented graphically in Figure 6.10. Two experiments were used for comparison. Experiment with an initial impact velocity of 7.1km/s which matches well with the simulation as pictured in Figure 6.10. On the other hand, the second experiment has an impact velocity of 7.2km/s, being marginally higher. Due to the negligible influence on the simulation results of such velocity change, both experiments are compared with one simulation.
An interesting feature of the experimental dataset is the large difference in the crater diameter in the second plate, with the 2nd being much smaller. This is likely caused by the presence of the multi-layer insulation material between the first and second plates. It is the only data point that had this feature indicated in the supplied data.

	Impact velocity [km/s]	1st bumper Hole Diameter [mm]	2nd bumper Hole Diameter [mm]
Exp 25	7.1	9.3	58
Simulation	7.1	9.1	52
Difference	-	-2.5%	-10.3%
Exp 25a	7.2	9	40
Simulation	7.1	9.1	52
Difference	-	1.1%	30%

Table 6.2: Results of simulation conducted at the velocity of 7.1 km/s, compared to experimental results. Experimental data acquired courtesy of Airbus Defence and Space GmbH.

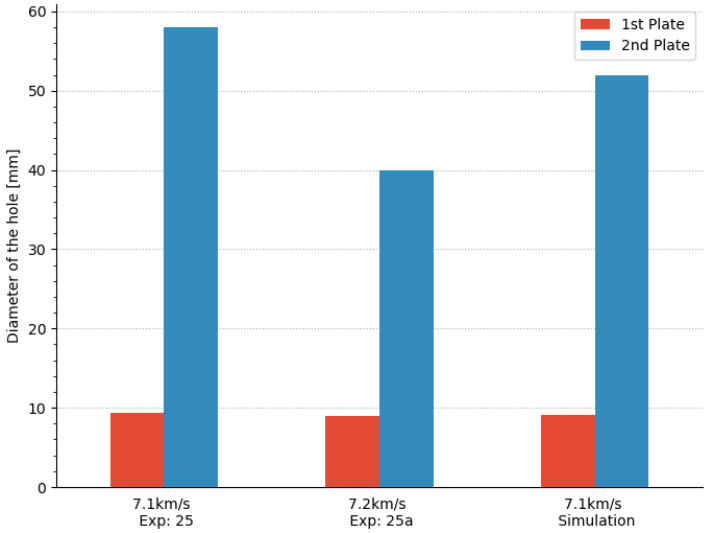

Figure 6.10: Result of the Simulation at the velocity of 7.1km/s. Experimental data acquired courtesy of Airbus Defence and Space GmbH.

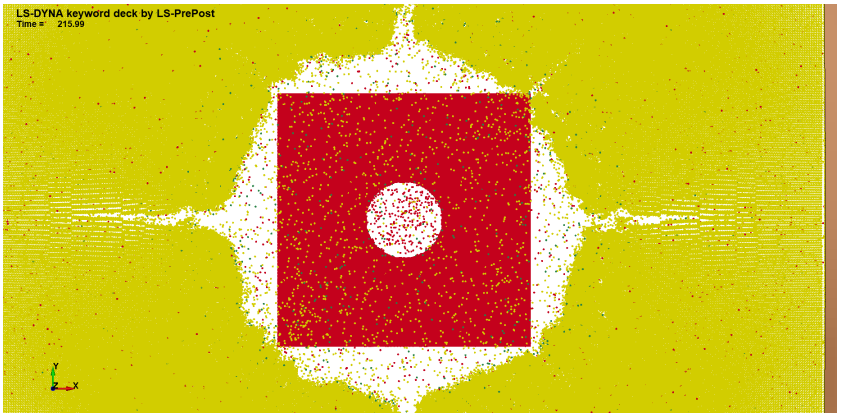

Figure 6.11: Crater of the 1st plate (red) and 2nd plate (yellow) at an impact velocity of 7.1km/s. Irregular shapes and cracks can be observed. Debris is seen in the background

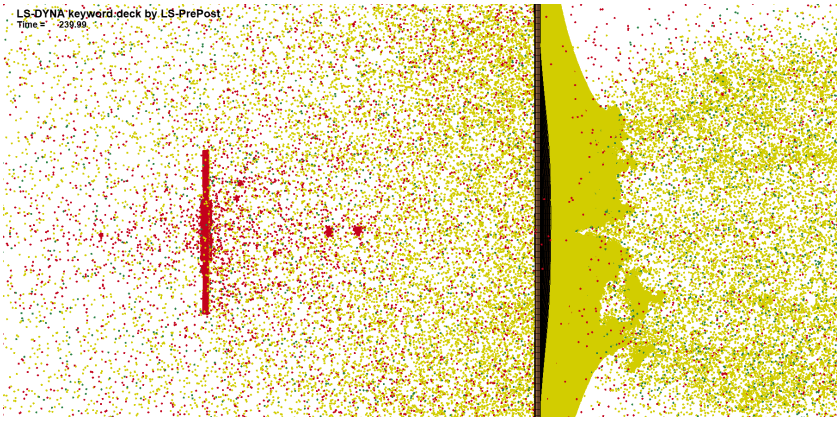

Figure 6.12: Side view of the aftermath of impact at 7.1km/s. Irregular edges and large deformation of the 2nd bumper can be observed, along with lots of debris in the vicinity of the impact zone.

6.4.2. Impact velocity = 5.4km/s

The impact at 5.4km/s corresponds to experiments 24 and 24a from the dataset. In this case, both experimental impacts have been conducted at the exactly same velocity and without multi-layer insulation between plates. The results from the experiments are very close to each other. The simulation achieves a corellation of up to 6% to the primary plate and up to 45% for the secondary plate crater size.

This simulation has been used for further comparisons of material models and EOS, due to a consistent set of experiments and relatively high discrepancy of the simulation from real-world data. Information on the comparisons is presented in section 6.5.

	Impact velocity [km/s]	1st bumper Hole Diameter [mm]	2nd bumper Hole Diameter [mm]
Exp 24	5.4	7.8	25
Simulation	5.4	8.25	35.5
Difference	-	5.8%	42%
Exp 24a	5.4	7.9	24
Simulation	5.4	8.25	35.5
Difference	-	4.4%	47.9%

Table 6.3: Results of the simulations conducted at 5.4 km/s compared to experimental results. Experimental data acquired courtesy of Airbus Defence and Space GmbH.

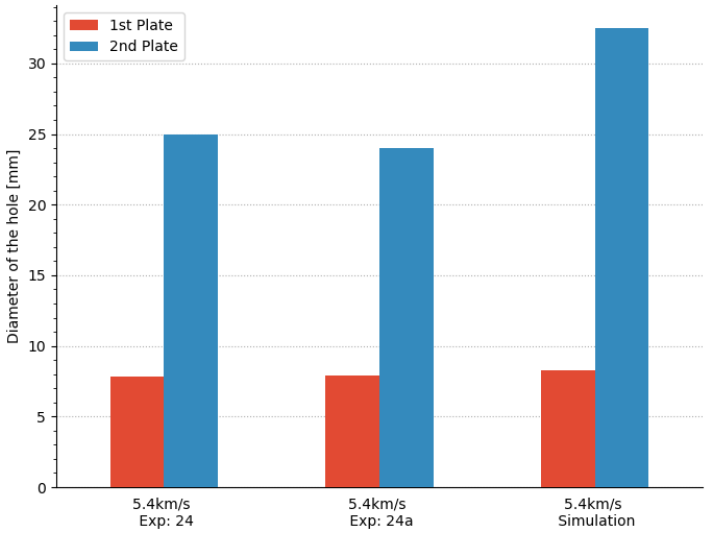

Figure 6.13: Comparison of results at an impact velocity of 5.4 km/s. Experimental data acquired courtesy of Airbus Defence and Space GmbH.

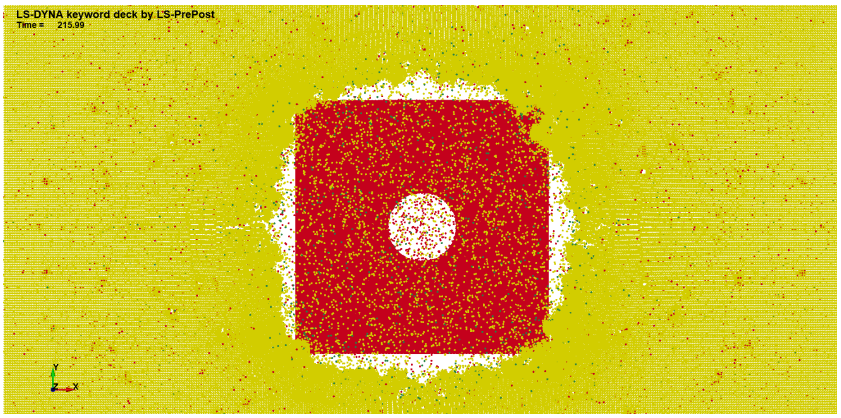

Figure 6.14: Crater of the 1st plate (red) and 2nd plate (yellow) at the impact velocity of 5.4km/s

6.4.3. Impact velocity = 3km/s

At the lowest impact velocity, two experiments are available. The velocity of 2.9km/s and 3.1km/s is examined. There is a large discrepancy in the measured results between those two data points. The slower projectile has created over 2 times greater crater in the second plate than the faster one, which is against the usual trend.

Therefore, two simulations were created to examine whether this behaviour could be simulated. The data from experiments and simulations are presented in the Table 6.4 and plotted in Figure 6.15. The simulation proved to have consistent results, without large differences for the two velocities examined. They were relatively close to the experiment at an impact speed of 2.9km/s, with marginal differences in the 1st crater diameter between the two. The view of both craters is pictured in Figure 6.16.

The experiment at an impact velocity of 3.1km/s is an outlier with a very small crater diameter. It could be caused by the inclusion of multi-layer isolation despite the lack of evidence for it. Moreover, it is the only experiment in the dataset that has data available on the velocity profile behind the second wall. This is presented in detail in section 6.3.

	Impact velocity [km/s]	1st bumper Hole Diameter [mm]	2nd bumper Hole Diameter [mm]
Exp 4.2	2.9	6.7	27
Simulation	2.9	7.5	25
Difference	-	10.7 %	-8.0 %
Exp 4.1	3.1	7	11
Simulation	3.1	7.1	25
Difference	-	1.4 %	127.3 %

Table 6.4: Results of the simulations conducted at 2.9km/ and 3.1km/s. Experimental data acquired courtesy of Airbus Defence and Space GmbH.

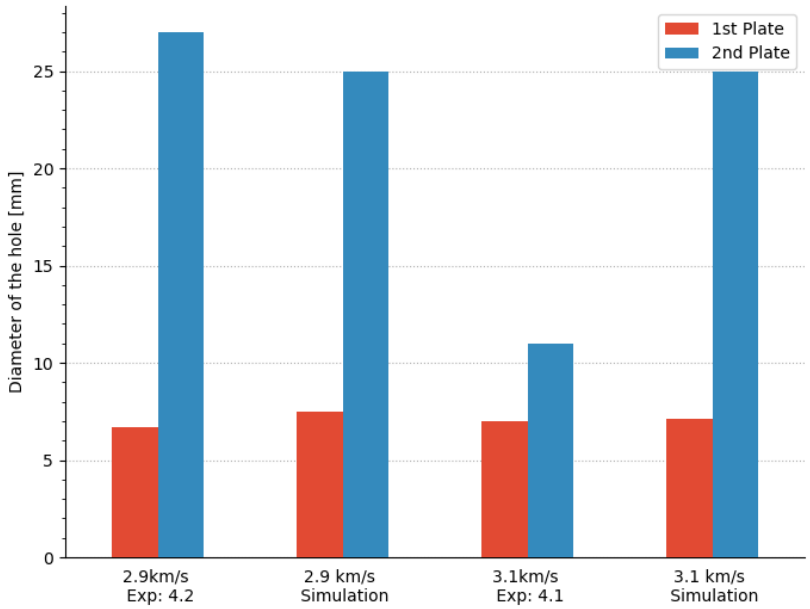

Figure 6.15: Comparison from experimental results to the simulation for experiments 4.1 and 4.2. Experimental data acquired courtesy of Airbus Defence and Space GmbH.

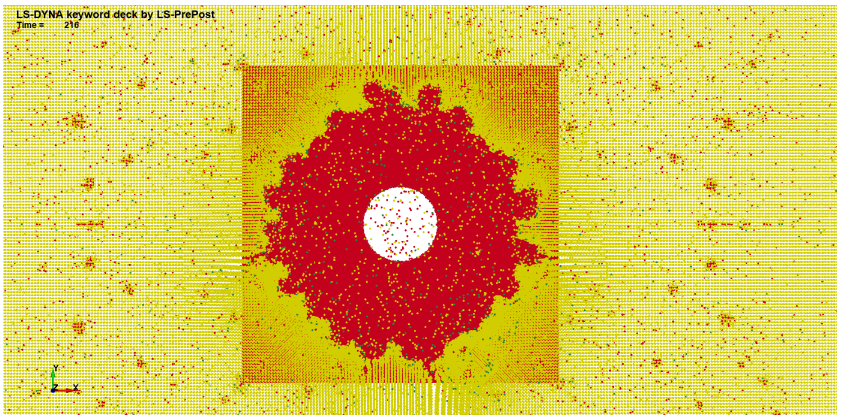

Figure 6.16: Crater of the 1st plate (red) and 2nd plate (yellow) at the impact velocity of 2.9 km/s

6.5. Comparison of inputs from different sources

Two different material models and EOS were compared. The Johnson-Cook material models were sourced from works from Lacome et al. [39] and FAA [46]. Mie-Gruneisen EOS were compared between one from Legaud et al. [37] and the second one by FAA[46]. The results are presented in Figure 6.18. An experiment with an impact velocity of 5.4 km/s was chosen for this comparison, as its initial accuracy was lower than others. Therefore, iteration was performed to examine whether parameters from other studies are more suitable for this velocity range. Moreover, the impact velocity of 5.4 km/s is in the middle of examined velocities.

It was observed, that parameters from two reliable sources on the same material have a negligible effect on the primary plate crater diameter. This effect is noticeable but minimal when the crater of the 2nd plate is compared—however, the shape of the damage zone in the 2nd plate changes depending on the parameters used as shown in Figure 6.17. The EOS sourced from Legaud et al. leads to a circular crater in the 2nd plate without any cracking. On the other side, data from FAA leads to a crater with a less circular shape with four radial cracks towards the corners of the plate. Using these experiments, it was determined the FAA [46] model has a better match to the experiments, by a small margin. The result in the middle of the two extremes was achieved by using the material model from FAA and EOS from the Legaud et al. study. This indicates that both EOS and Material models contribute towards the determination of the final result. For the remainder of the study, the values from FAA work are used as they showed the closest correlation with the experiments in this case.

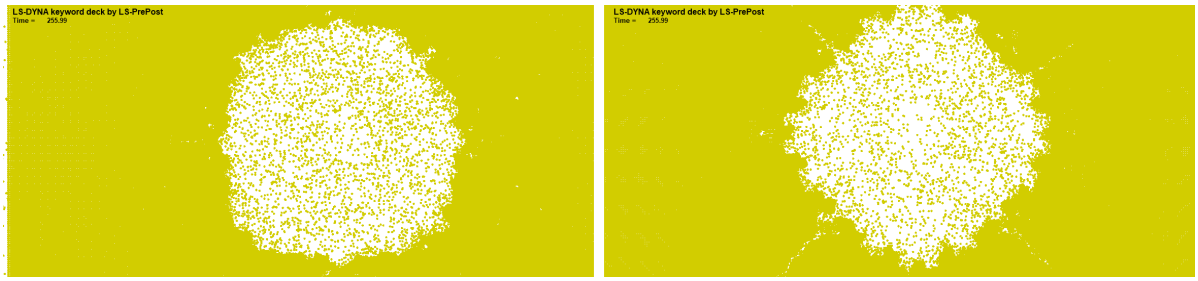

Figure 6.17: Difference in crater shape of the second plate between EOS from two different sources at an impact velocity of 5.4km/s. Gruneisen EOS from the Legaud et al. [37] (right) and one from FAA [46](left)

	Johnson-Cook Material Model	Mie Gruneisen EOS	1st bumper Hole Diameter [mm]	2nd bumper Hole Diameter [mm]
Exp 24	-	-	7.8	25
Simulation 1	Lacome et al.	Legaud et al.	8.4	37.7
Difference	-	-	7.7%	50%
Simulation 2	FAA	FAA	8.25	35.5
Difference	-	-	4.4%	42%
Simulation 3	FAA	Legaud et al.	8.4	37
Difference	-	-	7.7%	48%

Table 6.5: Comparison of results for different material models and EOS at an impact velocity of 5.4km/s. Experimental data acquired courtesy of Airbus Defence and Space GmbH.

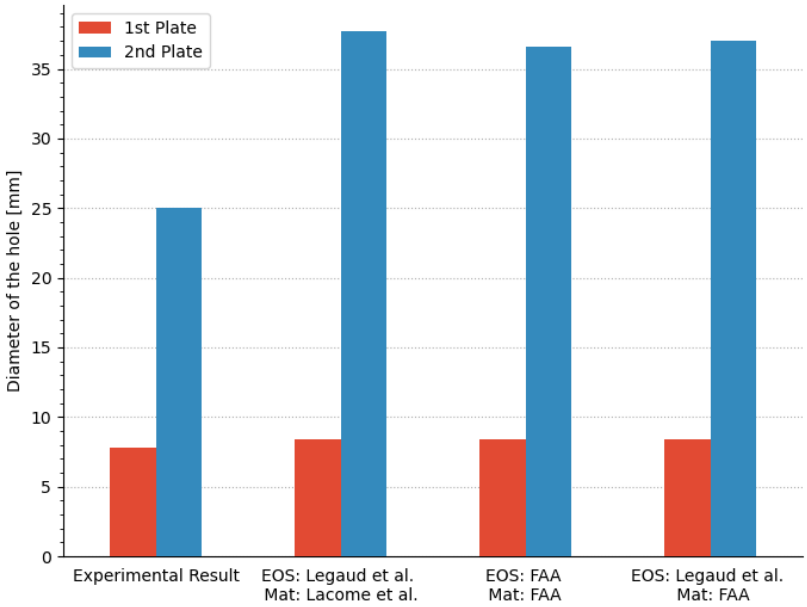

Figure 6.18: Comparison of results using different material models and equation of state. Two sources of material models are compared: Legaud et al. [37] and FAA [46]. Experimental data acquired courtesy of Airbus Defence and Space GmbH.

6.5.1. Material model fracutre parameters

The comparison was conducted to determine the influence of the fracture parameters on the result of the simulation. Those are optional parameters in LS-DYNA, that aid in representing fracture in some cases. The use of those parameters can influence the local failure, leading to the difference in the end crater size. For this, the Johnson-cook model from FAA [46] was used, as the full model was provided in the publication. The tests were conducted at the impact velocity of 5.4 km/s.The solution without the use of failure criteria describes the failure by plastic deformation or strain hardening, rather than fracture.

It was observed that the inclusion of failure criteria has led to a larger damage zone in the primary and secondary bumper. The most notable difference was observed in the 1st bumper, which is different to other iterations - the influence of others parameters was observed in the 2nd plate.

Overall the impact of the parameters on the results was negative. Most simulations predicted the diameter of the damage zone to be too big compared to experiments. The additional failure criteria have expanded this damage zone further. This is the expected result, as the addition of different ways for the structure to fail is likely to result in expanding the damage, rather than containing it.

Hole Diameter	1st bumper [mm]	2nd Bumper [mm]
Experimental Result	7.8	25
Without Fracture Criteria	8.25	32.5
Difference	5.8%	30%
With Fracture Criteria	8.9	33
Difference	14%	32%

Table 6.6: Results of comparison of simulation at 5.4km/s with and without fracture parameters. The accuracy is lower with the use of fracture. Experimental data acquired courtesy of Airbus Defence and Space GmbH.

6.6. Energy dissipated during impact

The energy balance is an important indication for any crash simulation. The law of conservation of energy shall be preserved. Numerical inaccuracy and approximations often lead to energy equations being not precisely balanced in the practical simulations, but this shall be minimized. The error is often deemed acceptable if it is in the range of 5%. The initial energy of the system is correct. It can be checked by manual computation of the kinetic energy of the projectile, as initially, this is the only object that moves. The kinetic energy is calculated using

$$E_k = \frac{mv^2}{2} = \frac{2\pi r \rho v^2}{3} \tag{6.1}$$

where r is the radius of the projectile, ρ is the density of the aluminium and v is the impact velocity. Using the formula for kinetic energy, the initial value of 849J is computed for an impact speed of 3.1km/s, 2576J for a speed of 5.4km/s and 4454 J for 7.1 km/s. Those values match exactly the initial energy state of the system at the beginning of respective simulations. However, simulations that are demonstrated in this work suffer from excessive energy loss that is beyond the usual, pictured in Figure 6.19. The highest energy loss is observed at the moment of impact of the debris cloud with the second plate. In that instant, over 50% of the total energy of the system is lost. During both impacts, a significant amount of kinetic energy is transformed into internal energy, which is expected. However, this conversion is not sufficient and therefore the major portion of the energy is lost.

This has been consulted with the developers of the LS-DYNA and has been confirmed that it is an error in the solver. In the used version R13.1-138 and prior, energy computation has been done using FE logic instead of a dedicated SPH one. As the Gruneisen EOS partly relies on internal energy to perform the computation, it is expected that an error is introduced because of this inconsistency. However, the error introduced is suspected by the developers to be mainly affecting the energy reading and not the displacement result. The developers scheduled an update with the fix of this issue at the beginning of the year 2023. In the meantime, several attempts were made to mitigate this issue with limited success.

The first attempt to make it more realistic is the inclusion of the thermal simulation. This had no noticeable effect on crater diameter or velocity, but it was suspected that the computation will have a beneficial effect on the energy balance. However, no effect was observed. Another method was the modification of the contact formulation between the Finite Elements and the SPH. The tied contact formulation could possibly cause some energy losses. However, this is not the primary cause as similar energy loss is observed for models that only include SPH particles.

It was determined that the major loss occurs when the SPH particles from one part interact with SPH from another part. There is a huge velocity difference between the two, and therefore a steep pressure gradient is present. It has been deducted that the artificial viscosity parameter can be responsible for this loss.

This has been tested by both changing the viscosity formulation and changing the viscosity parameters themselves. It was observed that the change of the formulation from Monaghan to Solid changed the shape of the energy plots, but the resulting values were kept identical. According to the LS-DYNA manual, the solid viscosity could potentially lead to lesser energy loss, but this was not observed in practice.

The difference was observed when the bulk viscosity parameters were altered. Both quadratic and linear parameters of the viscosity formula affect the energy loss, but also the stability of the simulation. It was determined that the reduction of the parameters leads to smaller energy loss but it did not eliminate the big drops that are responsible for the majority of the loss.

The inconsistency in energy balance was not noted in any examined LS-DYNA hypervelocity research. Previous studies did not consider energy balance as a parameter to be published. Therefore, it is a possibility that all previous research on this topic had this flaw that did go unnoticed.

As the majority of works focused on a single plate experiment, the total energy drop was still within the acceptable industry limits. Therefore, it might not cause much concern to the researchers. However, this drop is much larger when a double plate experiment is simulated, highlighting this issue.

Another option could be that previous versions of LS-DYNA did not have this problem. With no evidence of correct energy balance in the literature and note from developers that this has been an issue for a while, it is unlikely to be the case.

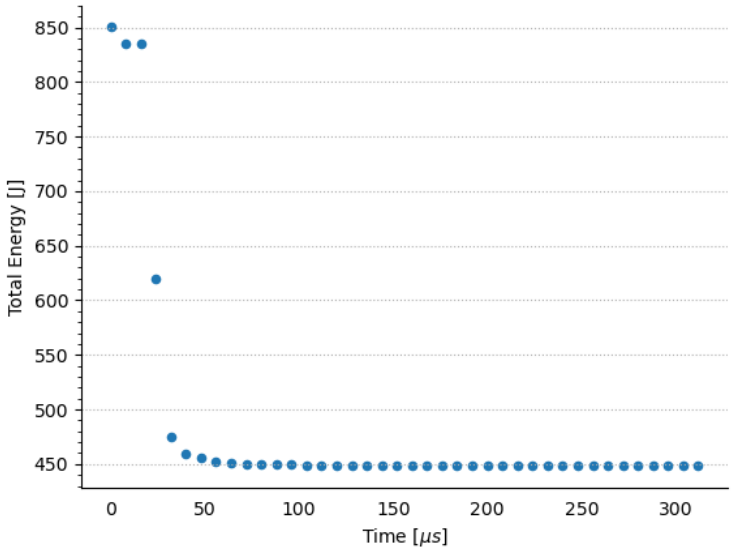

Figure 6.19: Plot describing the Total Energy of the system at the impact speed of 3.1km/s

6.7. Stress Field

In addition to the primary analysis, the stress on the surrounding structure was also evaluated as an auxiliary parameter. The Von Mises stress fringe plots were utilized to visualize the stress distribution in the structure. Despite the lack of experimental stress measurement data, the simulation results provide valuable insight into the stress conditions under three different impact velocities.

The stress field of the second plate was investigated. The stress in the first plate is not examined due to its small size and the different focus of the study. The stress is visible on the second plate once it is impacted by the debris cloud. It spreads from the middle in an approximately circular manner, until it hits the end of the plate. The interaction between waves can be observed by studying the stress, leading to peaks and valleys of stress within the structure. The limits of the fringe plot are set such that the red zones are near the yield strength of the material. Stress fields at the impact velocity of 7.1 and 5.4 km/s are displayed in Figure 6.20 and Figure 6.21 respectively. Similar behaviour can be noticed with a larger initial damage zone for impact with higher velocity. Waves in the plate for impact at 2.9 km/s are considerably less prominent as shown in Figure 6.22. The debris cloud impacts the second plate at different moments after the beginning of the simulation, due to varying cloud velocity. Therefore, the pictures are not taken at exactly the same time after contact with the second plate.

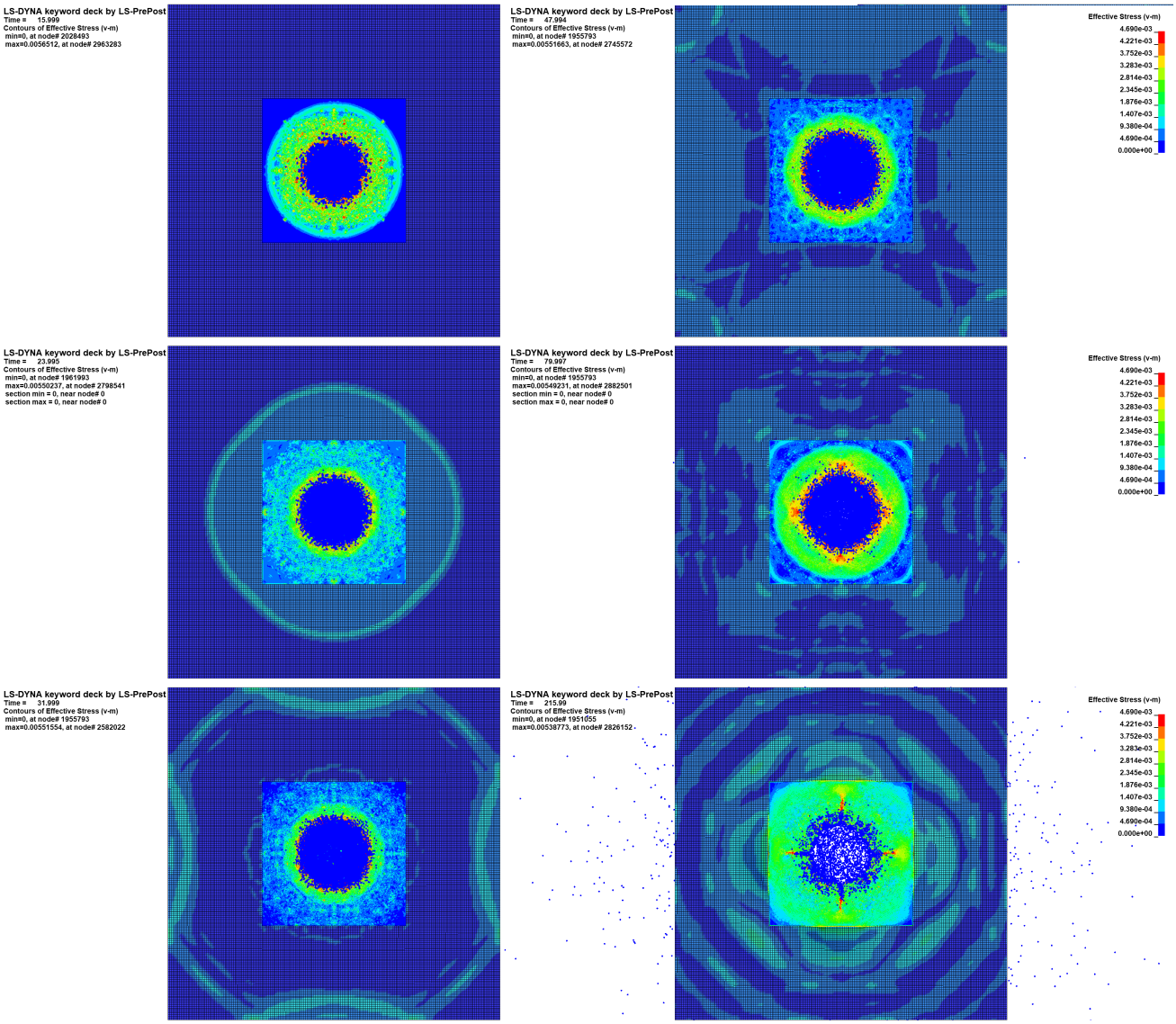

Figure 6.20: Von Mises stress field evolution fringe plots for the impact velocity of 7.1 km/s. The second plate is displayed with the stress in units of MegaBar.

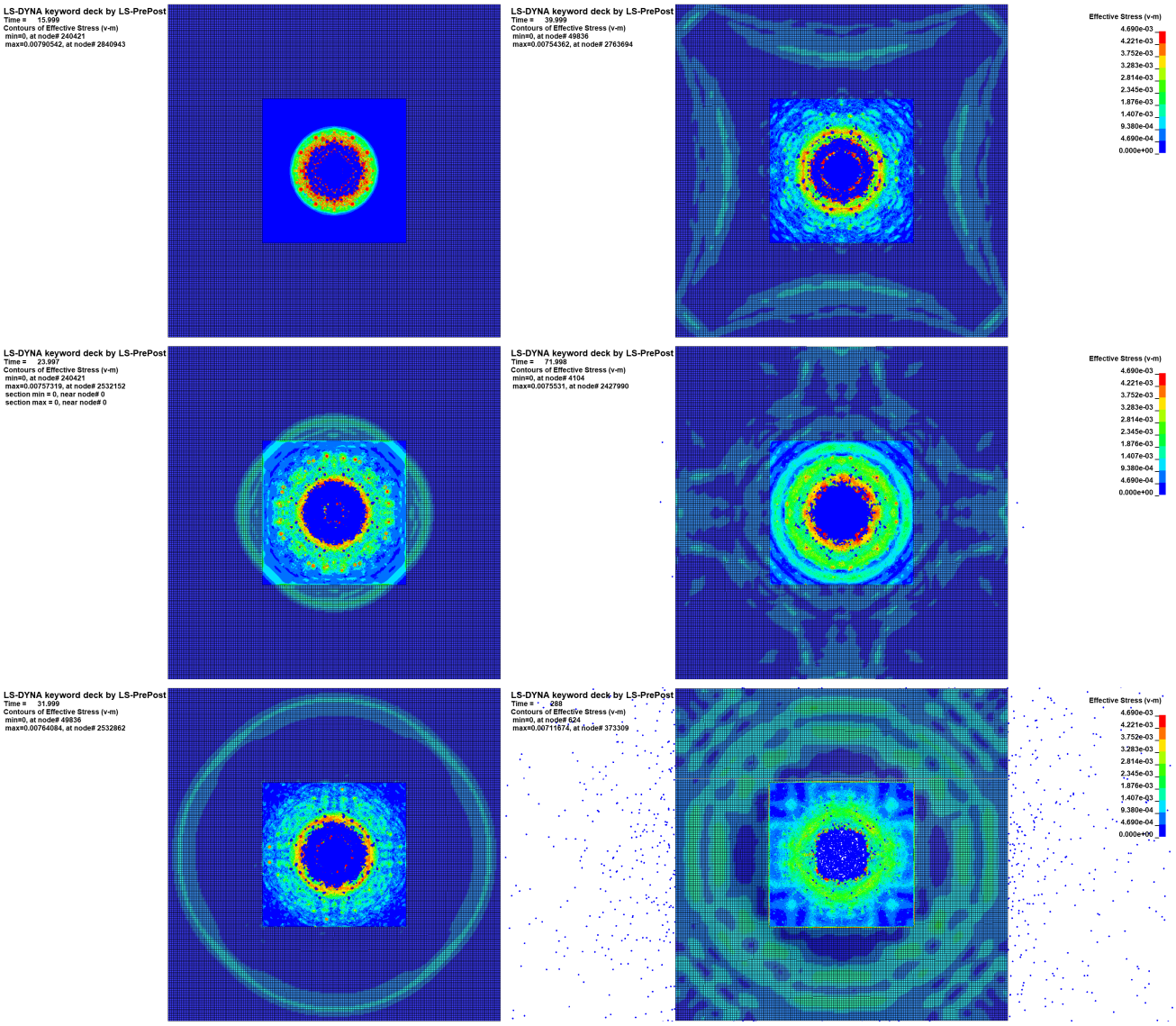

Figure 6.21: Von Mises stress evolution fringe plots for the impact velocity of 5.4 km/s.The second plate is displayed with the stress in units of MegaBar.

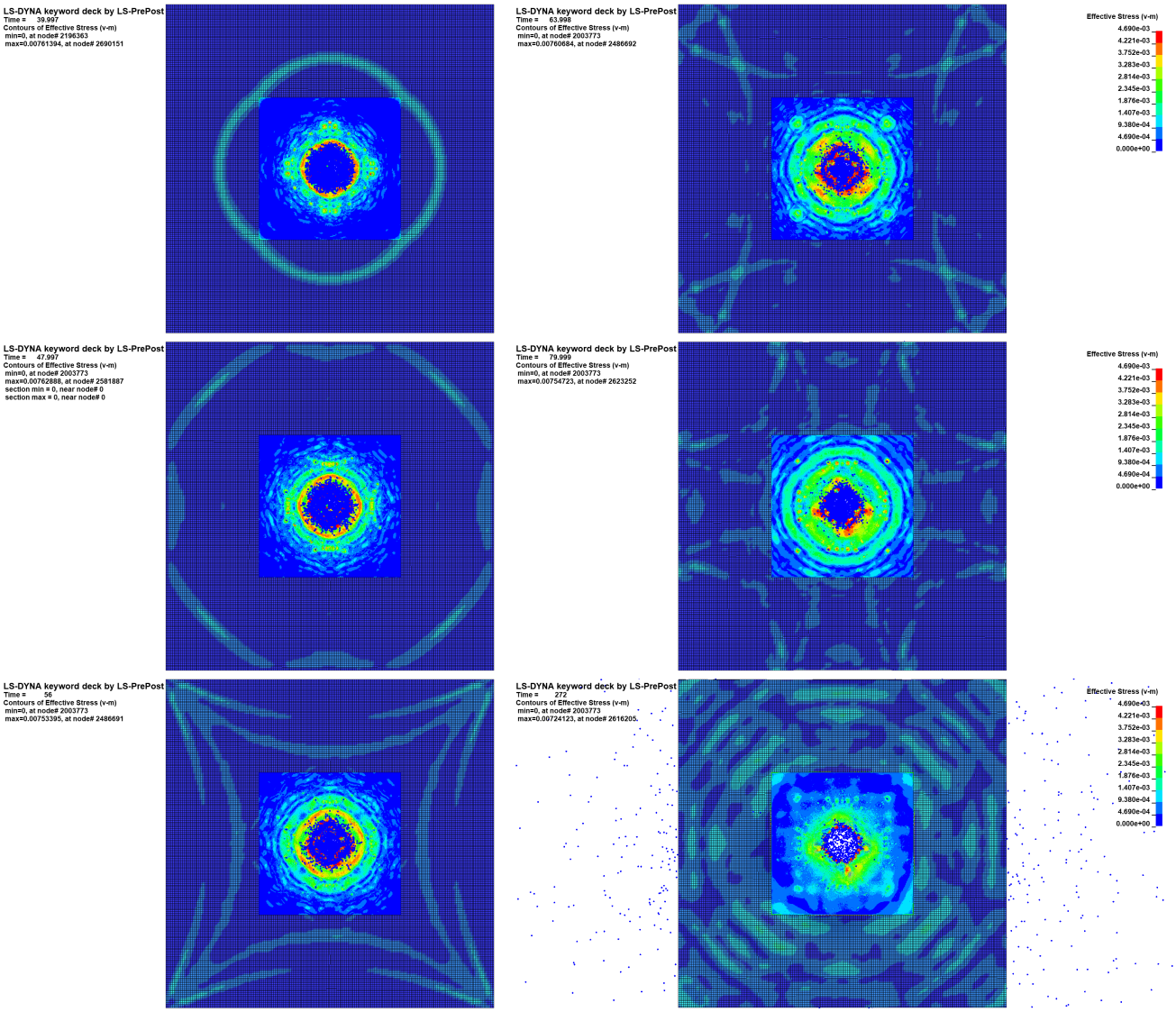

Figure 6.22: Von Mises stress evolution fringe plots for the impact velocity of 2.9 km/s.The second plate is displayed with the stress in units of MegaBar.

6.8. Analysis and Discussion

The general behaviour of the simulation shows follows the trends observed during the experiments. The formation of the ejecta veil and the primary debris cloud closely follows the shape observed in the literature. The interaction between the second plate and the debris cloud has proven to be the most challenging feature of the simulation.

It was observed that the velocity of the primary debris cloud is marginally slower than the initial hit. On the other hand, the second plate reduced the velocity of the debris cloud by as much as 80%, with the exception of singular particles. This confirms the effectiveness of the Whipple shield, especially at higher velocities. Both plates had equal and very small thicknesses, but the secondary plate slowed the debris cloud considerably. Therefore, the behaviour of the Whipple shield system as a whole has performed according to the expectations.

The accuracy of the simulation is the highest for the first plate. A very close match of up to 3% was observed for the 1st plate crater diameter for the velocity of 7.1km/s. For other simulations, the accuracy of that feature was well within 10 % of the experiments.

The crater diameter of the second plate is less consistent in the experimental results. As expected, the accuracy of the simulation is lower in this case. For all simulations with exception of one, the accuracy is within 30% of the original. The exceptionally big error has a value of 127% of the original value.

Aside from the inherent inaccuracy of the simulation, the experiment in consideration has an unusually low crater diameter - 11mm at 3.1 km/s impact. The neighbouring experiment at an impact velocity of 2.9 km/s has a crater diameter 2.45 times bigger - despite a lower impact velocity. The outlier could be explained by several things. The experiment could have had multi-layer insulation between bumpers, despite the lack of evidence in the experimental log. On the other hand, there could have been an error in the data acquisition. Finally, this variance could have been a testament to the unpredictability of the results of hypervelocity impacts.

7

Conclusion

A series of simulations on hypervelocity impacts were conducted. At first, the literature study was performed to determine the most suitable method for the simulation of such events and their history. It was determined that the SPH method offers the best accuracy when compared to other simulation techniques. It is also the most commonly used numerical technique used for such events.
From the gathered literature, the two most relevant studies were chosen to be replicated. The studies focused on SPH simulations validated in real-world experiments. They examined the effect of the impact on a single metal plate.
This was done as a way of developing the model from the ground up as the studies had less complex structures examined. The first study from Legaud et al. [37] focused on the crater diameter, whereas the second study from Plassard et al. [41] simulated stress-field around the impact zone. Both studies were replicated successfully with close matches to the originals.
The next step of the research is the model of a two-plate system. This has increased the computational complexity of the problem exponentially. The interaction between the primary debris cloud and the second plate requires a much larger plate model and CPU usage.
The simulations were conducted at three velocities that were also examined in the experiments provided by Airbus Defence and Space GmbH. Impacts at 2.9km/s, 5.4 km/s and 7.1km/s were examined. The spherical projectile with a 5 mm diameter impacted 1two plates with 0.8 mm thickness. The main output data from those experiments was the hole diameter formed in both the 1st and 2nd plates. All specimens in experiments were fully perforated.
The models were compared with the data from the double-plate experiments provided by ESA. The crater size in the first plate was very close to the original, within 2% at all velocities examined. The accuracy of the crater in the 2nd plate was less consistent.

7.1. Recommendations

There needs to be more research to fully explore the problem of space debris mitigation. This work focused on a small subset of problems related to hypervelocity impact. However, during the development of this research, multiple knowledge gaps were discovered that will need to be explored to make space travel safer and more sustainable.
Starting from the topics narrowly related to this research, the expansion of the number of simulated events would be beneficial to quantify the accuracy of the simulation. Currently, the simulation was compared to a dataset of 6 experiments, which had considerable variety. Expanding this pool would give more certainty in the simulation.
Moreover, a very specific projectile was used. Changes in dimensions or dimensions of the Whipple shield could create different results. To extrapolate the outcomes of the research, a more diverse pool of parts shall be examined.
The most relevant geometric change would be an examination of the triple-plate system. Such structures are commonly used in spacecraft, as the individual components are often in their own casing. Therefore, the debris has to penetrate a two-layer sandwich plus the casing itself. The development of

new Ballistic Limit Equations using triple-layer armour is outgoing. Numerical simulation of such events could enhance this research.
Another industry interest is in the stress field and vibrations caused by the impact. Those can pose a danger to other spacecraft components. As the shockwave propagates through the material, it could lead to failure in a much bigger area than the impact zone. Such simulations could be validated with the use of experiments that employ high-speed strain gauges on the target plates [49]. The use of the new version of LS-DYNA shall be investigated in order to correct the issues with the energy reading. This would enable accurate prediction of energy absorption within the plate, which would be crucial for correct stress field determination.
Data acquired from simulations could supplement the semi-empirical programs in the future. Currently, such software often bases its findings on the data from various experiments. However, the addition of data from numerical simulation could provide an effective way to tailor the prediction to the specific case.

References

[1] J. Rosenworcel, G. Starks, and N. Simington. *Federal Communications Commission*. Tech. rep. Washington: Federal Communications Commission, Sept. 2022.

[2] D. Mehrholz, L. Leushacke, W. Flury, R. Jehn, H. Klinkrad, and M. Landgraf. “Detecting, Tracking and Imaging Space Debris”. In: *ESA bulletin 109* (2002).

[3] S. Meng, L. Taddei, N. Lebaal, and S. Roth. *Advances in ballistic penetrating impact simulations on thin structures using Smooth Particles Hydrodynamics: A state of the art*. Feb. 2021. DOI: 10.1016/j.tws.2020.107206.

[4] W. D. Crozier and W. Hume. “High Velocity, Light Gas Gun”. In: *Journal of Applied Physics* 28.8 (Aug. 1957), pp. 892–894. DOI: 10.1063/1.1722882.

[5] H. F. Swift. “Light-Gas Gun Technology: A Historical Perspective”. In: *High-Pressure Shock Compression of Solids VIII*. Berlin/Heidelberg: Springer-Verlag, 2005, pp. 1–35. DOI: 10.1007/3-540-27168-6{_}1.

[6] A. J. Piekutowski. *Formation and Description of Debris Clouds Produced by Hypervelocity Impact*. NASA Contractor Report. George C. Marshall Space Flight Center, 1996.

[7] A. J. Piekutowski. “Holes produced in thin aluminum sheets by the hypervelocity impact of aluminum spheres”. In: *International Journal of Impact Engineering* 23.1 PART II (1999), pp. 711–722. DOI: 10.1016/S0734-743X(99)00116-5.

[8] M. J. Forrestal and A. J. Piekutowski. “Penetration experiments with 6061-T6511 aluminum targets and spherical-nose steel projectiles at striking velocities between 0.5 and 3.0 km/s”. In: *International Journal of Impact Engineering* 24.1 (2000), pp. 57–67. DOI: 10.1016/S0734-743X(99)00033-0.

[9] A. J. Piekutowski. “Debris clouds produced by the hypervelocity impact of nonspherical projectiles”. In: *International Journal of Impact Engineering* 26.1-10 (2001), pp. 613–624. DOI: 10.1016/S0734-743X(01)00122-1.

[10] A. J. Piekutowski, K. L. Poormon, E. L. Christiansen, and B. A. Davis. “Performance of whipple shields at impact velocities above 9 km/s”. In: *International Journal of Impact Engineering* 38.6 (June 2011), pp. 495–503. DOI: 10.1016/J.IJIMPENG.2010.10.021.

[11] J. A. Rogers, P. T. Mead, K. Harrison, K. R. Kota, J. D. Leaverton, G. Lukasik, W. Kulatilaka, J. W. Wilkerson, and T. E. Lacy. “Hypervelocity impact response of polyethylene plates”. In: *AIAA Scitech 2021 Forum* (2021), pp. 1–10. DOI: 10.2514/6.2021-0887.

[12] S. Khatiwada, C. A. Armada, and E. V. Barrera. “Hypervelocity impact experiments on epoxy/ultra-high molecular weight polyethylene fiber composites reinforced with single-walled carbon nanotubes”. In: *Procedia Engineering*. Vol. 58. Elsevier Ltd, 2013, pp. 4–10. DOI: 10.1016/j.proeng.2013.05.003.

[13] W. H. Choi, H. S. Choe, and Y. W. Nam. “Space hypervelocity impact-shielding and microwave absorbing composite composed of cobalt-coated aramid fibers”. In: *Composite Structures* 266 (June 2021), p. 113875. DOI: 10.1016/J.COMPSTRUCT.2021.113875.

[14] E. Giannaros, A. Kotzakolios, V. Kostopoulos, and G. Campoli. “Hypervelocity impact response of CFRP laminates using smoothed particle hydrodynamics method: Implementation and validation”. In: *International Journal of Impact Engineering* 123 (Jan. 2019), pp. 56–69. DOI: 10.1016/J.IJIMPENG.2018.09.016.

[15] F. Angrilli, D. Pavarin, M. De Cecco, and A. Francesconi. “Impact facility based upon high frequency two-stage light-gas gun”. In: *Acta Astronautica* 53.3 (Aug. 2003), pp. 185–189. DOI: 10.1016/S0094-5765(02)00207-2.

[16] R. Vignjević and N. Đorđević. “Modelling of High Velocity Impact on Carbon Fibre Composite Materials”. In: *Scientific Technical Review* 60 (2010), pp. 20–31.

[17] Z. L. Zhang, T. Ma, D. L. Feng, and M. B. Liu. “A New Formula for Predicting the Crater Size of a Target Plate Produced by Hypervelocity Impact”. In: *International Journal of Computational Methods* 17.1 (Feb. 2020). DOI: 10.1142/S0219876218440048.

[18] A. Jackson, P. Krisko, P. Anz-Meador, A. Bade, A. A. Jackson, R. C. Reynolds, P. Eichler, M. Matney, P. D. Anz-Meador, and N. L. Johnson. “Breakup model update at nasa/jsc”. In: (2000).

[19] N. Cimmino, G. Isoletta, R. Opromolla, G. Fasano, A. Basile, A. Romano, M. Peroni, A. Panico, and A. Cecchini. “Tuning of NASA standard breakup model for fragmentation events modelling”. In: *Aerospace* 8.7 (July 2021). DOI: 10.3390/aerospace8070185.

[20] J. Murray, H. Cowardin, J.-C. Liou, M. Sorge, N. Fitz-Coy, and T. Huynh. “Analysis of the DebriSat Fragments and Comparison to the NASA Standard Satellite Breakup Model”. In: *International Orbital Debris Conference*. Sugar Land, 2019.

[21] D. Mains and M. Sorge. “Integrated breakup modeling solutions from debrisat analysis”. In: *Journal of Space Safety Engineering* 7.3 (Sept. 2020), pp. 230–234. DOI: 10.1016/J.JSSE.2020.07.024.

[22] M. E. Sorge. “Satellite Fragmentation Modeling with IMPACT”. In: *AIAA/AAS Astrodynamics Specialist Conference and Exhibit*. Honolulu: American Institute of Aeronautics and Astronautics, Inc., Aug. 2008. DOI: 10.2514/6.2008-6265.

[23] F. Hoots and M. Sorge. “Satellite Breakup Parameter Determination”. In: *The Journal of the Astronautical Sciences* 59.1-2 (June 2012), pp. 120–140. DOI: 10.1007/s40295-013-0009-2.

[24] S. Kempf, F. Schäfer, M. Rudolph, N. Welty, T. Donath, R. Destefanis, L. Grassi, R. Janovsky, L. Evans, and A. Winterboer. “Risk and vulnerability analysis of satellites due to mm/sd with PIRAT”. In: (2013), pp. 22–25.

[25] F. K. Schäfer, S. Ryan, M. Lambert, and R. Putzar. “Ballistic limit equation for equipment placed behind satellite structure walls”. In: *International Journal of Impact Engineering* 35.12 (2008), p. 1784. DOI: 10.1016/j.ijimpeng.2008.07.074{\"{i}}.

[26] A. Francesconi, C. Giacomuzzo, L. Olivieri, G. Sarego, A. Valmorbida, M. Duzzi, K. D. Bunte, E. Farahvashi, T. Cardone, and D. de Wilde. “Numerical simulations of hypervelocity collisions scenarios against a large satellite”. In: *International Journal of Impact Engineering* 162 (Apr. 2022). DOI: 10.1016/j.ijimpeng.2021.104130.

[27] A. Francesconi, C. Giacomuzzo, L. Olivieri, G. Sarego, M. Duzzi, F. Feltrin, A. Valmorbida, K. D. Bunte, M. Deshmukh, E. Farahvashi, J. Pervez, M. Zaake, T. Cardone, and D. de Wilde. “CST: A new semi-empirical tool for simulating spacecraft collisions in orbit”. In: *Acta Astronautica* 160 (July 2019), pp. 195–205. DOI: 10.1016/j.actaastro.2019.04.035.

[28] F. H. Harlow. “Numerical Fluid Dynamics”. In: *The American Mathematical Monthly* 72.sup2 (Feb. 1965), pp. 84–91. DOI: 10.1080/00029890.1965.11970702.

[29] J. Monaghan and Gingold RA. “Smoothed particle hydrodynamics - theory and application to non-spherical stars”. In: *Monthly Notices of the Royal Astronomical Society* 181.3 (1977). DOI: https://doi.org/10.1093/mnras/181.3.375.

[30] J. Monaghan, M. Stromlo, and S. Spring Obs. “Shock Simulation by the Particle Method SPH”. In: *Journal Of Computational Physics* 52 (1983), pp. 374–389.

[31] J. R. Pasta and S. Ulam. “Heuristic numerical work in some problems of hydrodynamics”. In: *Mathematical tables and other aids to computation* 13.65 (1959), pp. 1–12.

[32] K. Wen and X. W. Chen. “Failure evolution in hypervelocity impact of Al spheres onto thin Al plates”. In: *International Journal of Impact Engineering* 147 (Jan. 2021). DOI: 10.1016/j.ijimpeng.2020.103727.

[33] S. Signetti and A. Heine. “Transition regime between high-velocity and hypervelocity impact in metals – A review of the relevant phenomena for material modeling in ballistic impact studies”. In: *International Journal of Impact Engineering* (Sept. 2022), p. 104213. DOI: 10.1016/j.ijimpeng.2022.104213.

[34] M. B. Liu and G. R. Liu. “Smoothed Particle Hydrodynamics (SPH): an Overview and Recent Developments”. In: *Archives of Computational Methods in Engineering* 17.1 (Mar. 2010), pp. 25–76. DOI: 10.1007/s11831-010-9040-7.

[35] M. S. Bartlett. “Statistical Estimation of Density Functions”. In: *The Indian Journal of Statistics, Series A* 25.3 (1961), pp. 245–254.

[36] Y. Xiao, H. Wu, and X. Ping. “On the simulation of fragmentation during the process of ceramic tile impacted by blunt projectile with SPH method in LS-DYNA”. In: *CMES - Computer Modeling in Engineering and Sciences* 122.3 (2020), pp. 923–954. DOI: 10.32604/cmes.2020.07686.

[37] T. Legaud, M. Le Garrec, N. Van Dorsselaer, and V. Lapoujade. *Improvement of satellites shielding under high velocity impact using advanced SPH method*. Tech. rep. 2019.

[38] J.-M. Sibeaud, P. Héreil, and V. Albouys. “Hypervelocity Impact on Spaced Target Structures: Experimental and Ouranos Simulation Achievements”. In: *International Journal of Impact Engineering* 29.1-10 (Dec. 2003), pp. 647–658. DOI: 10.1016/j.ijimpeng.2003.10.012.

[39] J. L. Lacome, C. Espinosa, and C. Gallet. *Simulation of Hypervelocity Spacecrafts And Orbital Debris Collisions using Smoothed Particle Hydrodynamics in LS-DYNA*. Tech. rep.

[40] T. Legaud, H. Abdulhamid, P. Deconinck, M. Le Garrec, and V. Lapoujade. “Use of Prepreg Carbon and Aluminum in Satellite Shielding Submitted to High Velocity Impacts”. In: *6 th International LS-DYNA ® Users Conference*. 2020, pp. 1–12.

[41] F. Plassard, J. Mespoulet, and P. Hereil. *Hypervelocity impact of aluminium sphere against aluminium plate : experiment and LS-DYNA correlation*. Tech. rep. Puybrun: Thiot Ingenierie, 2011.

[42] X. Huang, C. Yin, H. Ru, S. Zhao, Y. Deng, Y. Guo, and S. Liu. “Hypervelocity impact damage behavior of B4C/Al composite for MMOD shielding application”. In: *Materials and Design* 186 (Jan. 2020). DOI: 10.1016/j.matdes.2019.108323.

[43] V. Hohler and A. Stilp. “Hypervelocity impact of rod projectiles with L/D from 1 to 32”. In: *International Journal of Impact Engineering* 5.1-4 (Jan. 1987), pp. 323–331. DOI: 10.1016/0734-743X(87)90049-2.

[44] V. Hohler and A. Stilp. “Hypervelocity impact of rod projectiles with L/D from 1 to 32”. In: *International Journal of Impact Engineering* 5.1-4 (Jan. 1987), pp. 323–331. DOI: 10.1016/0734-743X(87)90049-2.

[45] Z. Guo, S. Martinez-Morales, and W. Chen. “Projectile strength effects on the ballistic impact response of soft armor targets”. In: *Textile Research Journal* 90.3-4 (Feb. 2020), pp. 282–293. DOI: 10.1177/0040517519862882.

[46] Federal Aviation Administration. *Explicit Finite Element Analysis of 2024-T3/T351 Aluminum Material Under Impact Loading for Airplane Engine Containment and Fragment Shielding*. Tech. rep. Washington, 2008.

[47] I. Gkolfinopoulos and N. Chijiwa. “Determination of Johnson–Cook Material and Failure Model Constants for High-Tensile-Strength Tendon Steel in Post-Tensioned Concrete Members”. In: *Applied Sciences (Switzerland)* 12.15 (Aug. 2022). DOI: 10.3390/app12157774.

[48] J. P. Morris and J. J. Monaghan. “A Switch to Reduce SPH Viscosity”. In: *Journal of Computational Physics* 136.1 (Sept. 1997), pp. 41–50. DOI: 10.1006/JCPH.1997.5690.

[49] K. Ueda and A. Umeda. *Dynamic Response of Strain Gages up to 300 kHz*. Tech. rep. Tsukuba: National Research Laboratory of Metrology, 1997.

8

Appendix 1: Version Log

8.1. Replication of Plassard et al.

No.	Change	Result
0	Basic Version - JC - Wrong Timestep	Crash
1	Timestep Change (Wrong) with Hydro Model	
2	Correct Timestep with JC Model	Inaccurate
3	Fix to the Grueinsen EOS	
4	Correct Timestep with Hydro Model	
5	Experimentation with different JC model Parameters (ESA)	
6	Addition o the Pressure cut-off value from the initial JC model to ESA JC model	
7	Removal of Erosion Criteria from ESA material model	
8	Change to EOS and material model directly provided by reference.	
9	Use of load curve for the capture of the model at given states	
9	Deletion of default information capture interval	
10	Fix of the Load curve definition	
11	Change of Contact Stiffness and sliding friction coefficient	Improvement
12	Creation of half-model version with symmetry plane	
13	Addition of the fixed BC around the plate	
14	Attempt to use type 43 element formulation for solids instead of default 0	Crash
15	Attempt to use type 45 element formulation for solids instead of default 0	
16	Attempt to use type 1 element formulation for solids instead of default 0	
17	Attempt to use type 45 element formulation for solids instead of default 0	
18	Attempt to use type 47 element formulation for solids instead of default 0	
19	Deletion of the previous contact settings	
20	Addition of DEFINE_ADAPTIVE_SOLID_TO_SPH keyword	Improvement
21	Use of fully intergrated elements for Solid	
22	Corrected definition of the adaptive connection keyword	
23	Reintroduction of Contact settings	Best

Table 8.1: The list of performed iterations for the replication of the study from Plassard et al.

9

Appendix 2: LS-DYNA Keywords

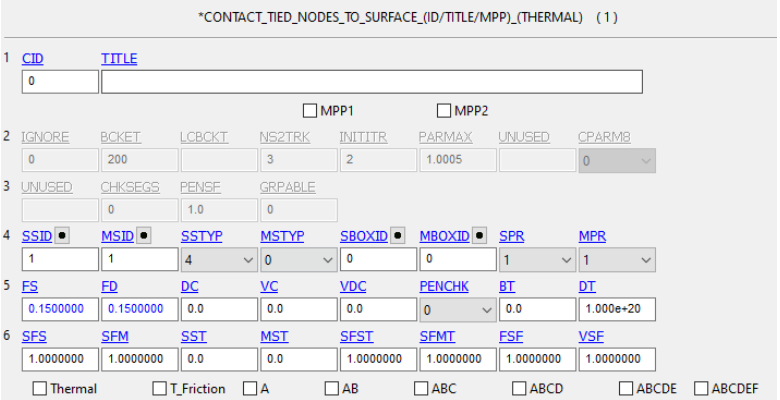

Figure 9.1: Contact Keyword for the connection of SPH to FEM

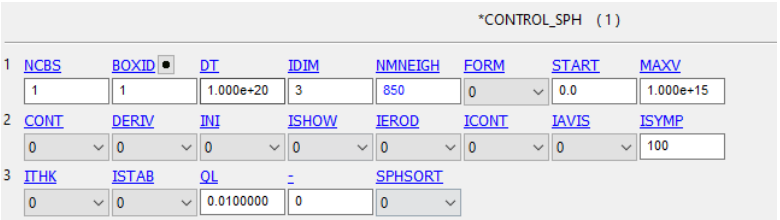

Figure 9.2: Control SPH keyword

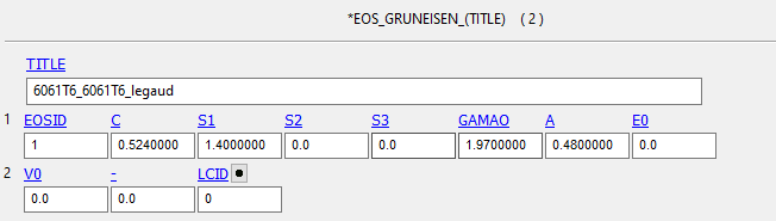

Figure 9.3: Gruneisen EOS parameters sourced from Legaud et al. [37]

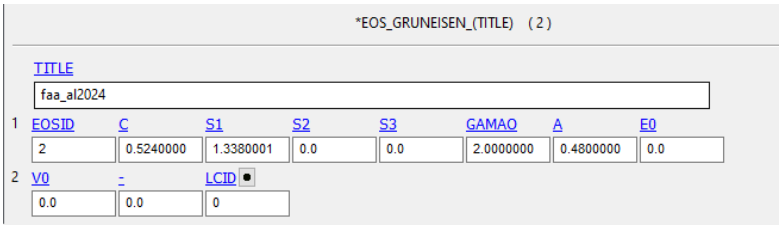

Figure 9.4: Gruneisen EOS parameters sourced from FAA [46]

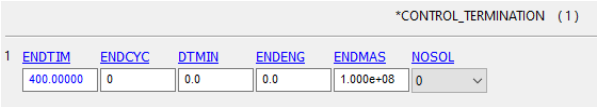

Figure 9.5: Termination Setting keyword

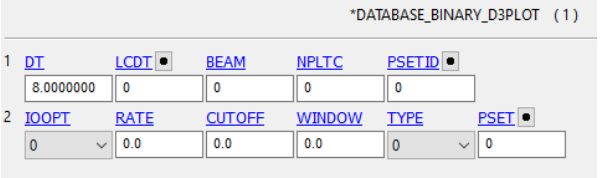

Figure 9.6: Keyword for the setting of extracted framerate

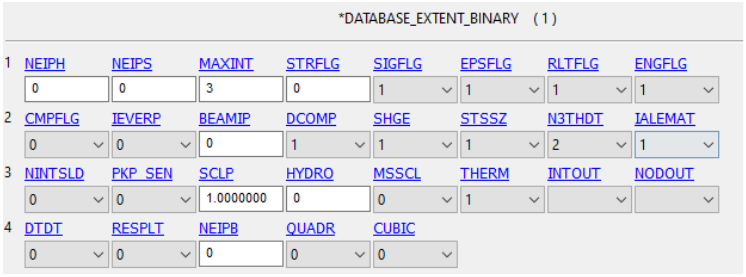

Figure 9.7: Output setting keyword

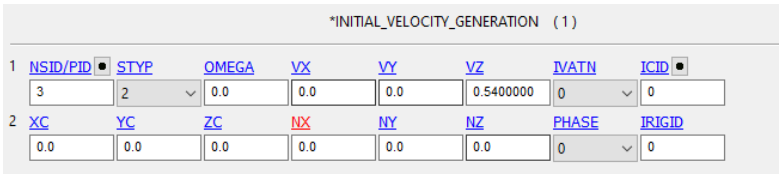

Figure 9.8: Initial velocity setting keyword

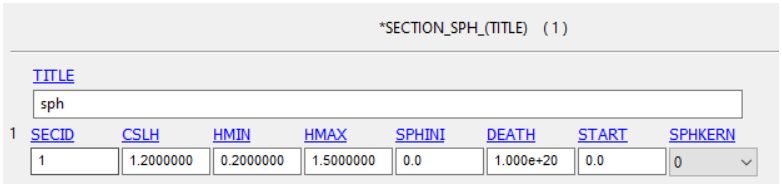

Figure 9.9: Section setting keyword for SPH

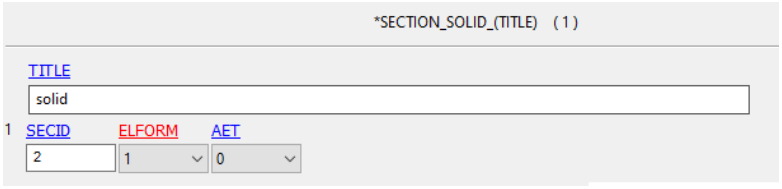

Figure 9.10: Section setting keyword for FE